Inorganic Chemistry
Article

Inorg. Chem. **2009**, *48*, 7033–7047 **7033**
DOI: 10.1021/ic802252k

Systematic Study of Spin Crossover and Structure in $[Co(terpyRX)_2](Y)_2$ Systems (terpyRX = 4′-alkoxy-2,2′:6′,2″-terpyridine, X = 4, 8, 12, Y = BF_4^-, ClO_4^-, PF_6^-, BPh_4^-)

Pia Nielsen,[†] Hans Toftlund,*[,†] Andrew D. Bond,[†] John F. Boas,[‡] John R. Pilbrow,[‡] Graeme R. Hanson,[∥] Christopher Noble,[∥] Mark J. Riley,[⊥] Suzanne M. Neville,[§] Boujemaa Moubaraki,[§] and Keith S. Murray*[,§]

[†]*Institute of Physics and Chemistry, University of Southern Denmark, Odense, Denmark, and* [‡]*School of Physics and* [§]*School of Chemistry, Monash University, Clayton, Victoria 3800, Australia,* [∥]*Centre for Magnetic Resonance and* [⊥]*School of Chemistry and Molecular Biosciences, University of Queensland, St. Lucia, Queensland 4072, Australia*

Received November 23, 2008

A family of spin crossover cobalt(II) complexes of the type $[Co(terpyRX)_2](Y)_2 \cdot nH_2O$ (X = 4, 8, 12 and Y = BF_4^-, ClO_4^-, PF_6^-, BPh_4^-) has been synthesized, whereby the alkyl chain length, RX, and counteranion, Y, have been systematically varied. The structural (single crystal X-ray diffraction) and electronic (magnetic susceptibility, electron paramagnetic resonance (EPR)) properties have been investigated within this family of compounds. Single crystal X-ray diffraction analysis of $[Co(terpyR8)_2](ClO_4)_2$, $[Co(terpyR8)_2](BF_4)_2 \cdot H_2O$, and $[Co(terpyR4)_2](PF_6)_2 \cdot 3H_2O$, at 123 K, revealed compressed octahedral low spin Co(II) environments and showed varying extents of disorder in the alkyl tail portions of the terpyRX ligands. The magnetic and EPR studies were focused on the BF_4^- family and, for polycrystalline solid samples, revealed that the spin transition onset temperature (from low to high spin) decreased as the alkyl chain lengthened. EPR studies of polycrystalline powder samples confirmed these results, showing signals only due to the low spin state at the temperatures seen in magnetic measurements. Further to this, simultaneous simulation of the EPR spectra of frozen solutions of $[Co(terpyR8)_2](BF_4)_2 \cdot H_2O$, recorded at S-, X-, and Q-band frequencies, allowed accurate determination of the *g* and *A* values of the low spin ground state. The temperature dependence of the polycrystalline powder EPR spectra of this and the R4 and R12 complexes is explained in terms of Jahn−Teller effects using the warped Mexican hat potential energy surface model perturbed by the low symmetry of the ligands. While well recognized in Cu(II) systems, this is one of the few times this approach has been used for Co(II).

Introduction

One of the most challenging areas in the study of spin crossover (SCO) materials is that dealing with supramolecular/intermolecular solid state effects occurring between the constituent *d*block ions, such as Fe(II) or Co(II), surrounded by their particular ligand environment. Not only have ligand−ligand interactions, such as $\pi-\pi$ effects, been recognized as being able to influence the spin transition temperature, $T_{1/2}$ (the temperature at which the high spin, HS, and low spin, LS, molecules are in 50:50 ratio) and the shape and hysteretic (memory) nature of the spin transition curve, but ligand−solvate, anion−solvate, and anion−ligand interactions are now known to play important roles, often involving hydrogen bonding.[1−4] However, such intermolecular interactions are difficult to control or predict, in particular when multiple interactions are present. As such, one of the best approaches to investigate these solid state effects is to carry out systematic studies where one feature, such as an anion or solvate molecule, is varied and the magnetic and structural consequences followed.

For Co(II), the d^7 $S = 3/2$ to 1/2 spin transition is known to occur in materials of the type $[Co(terpy)_2](Y)_2 \cdot zH_2O$ (Y = halide, pseudohalide, NO_3^-, ClO_4^-, z = 0−5), where the magnetic properties associated with such complexes are both

*To whom correspondence should be addressed. E-mail: keith.murray@sci.monash.edu.au. Tel: +61-3-99054512. Fax: +61-3-99054597. E-mail: hto@ifk.sdu.dk. Fax: +45 6615 8780. Tel: +45 6550 2543.

(1) Gütlich, P.; Goodwin, H. A. *Top. Curr. Chem.* **2004**, 233–235 see review articles in this multivolume series.

(2) Leita, B; Neville, S. M.; Halder, G. J.; Moubaraki, B; Kepert, C. J.; Létard, J.F.; Murray, K. S. *Inorg. Chem.* **2007**, *46*, 8784–8795 and references therein.

(3) Moubaraki, B; Leita, B. A.; Halder, G. J.; Batten, S. R.; Jensen, P.; Smith, J. P.; Cashion, J. D.; Kepert, C. J.; Létard, J.F.; Murray, K. S. *Dalton Trans.* **2007**, 4413–4426.

(4) Elhaïk, J.; Kilner, M. A.; Halcrow, M. *Dalton Trans.* **2006**, 823–830 and references cited therein to related work by the authors dealing with supramolecular effects.

Published on Web 07/02/2009

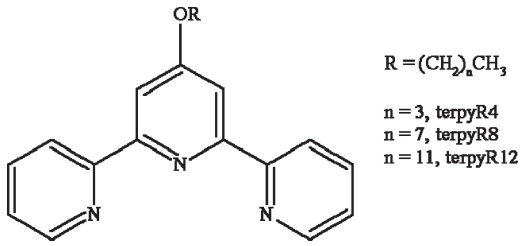

Figure 1. TerpyRX ligand, where X = 4, 8, and 12.

anion and solvent dependent.[5−9] This is highlighted in a recent example by Real and coworkers where analogous Co(II)4terpyridone (terpyOH) complexes display spin transitions sensitive to both solvent and anion.[10] This family of terpyOH ligands has been further extended here, to include long alkyl chains bonded at the oxygen in the 4position of the central pyridine ring (Figure 1), to form a series of complexes of the type $[Co(terpyRX)_2](Y)_2$, where X = 4, 8, 12 and Y = ClO_4^-, BF_4^-, PF_6^-, BPh_4^-. In comparison to other ligand related intermolecular influences, the crystal packing and magnetic effects of long alkyl chains situated at the periphery of the metal−ligand centers are less well studied.[11] However, Hayami and coworkers have previously reported longer chain members of this terpyRX family, in which X = 14 and 16, and Y = BF_4^-, where notably the nonsolvated versions were reported to display unusual, abrupt "reverse" spin transitions for X = 14 and 16, at 217 and 250 K, respectively.[12] Of note, these abrupt transitions coincided with a structural phase transition and display an unusual "undulating" μ_{eff} behavior as a function of temperature. In contrast, the solvated phase $[Co(terpyR16)_2](BF_4)_2 \cdot MeOH$ was found to display a broad, gradual, and incomplete transition, similar to those of the $Co(terpyridone)_2$ NO_3^- and BF_4^-/SiF_6^{2-} salts[10] and the present hydrated/solvated species (vide infra). Very recently, this group reported that $[Co(terpyR14)_2](BF_4)_2 \cdot MeOH$ showed a rather abrupt $S = 3/2$ to 1/2 spin transition at 50 K and a transition between two HS states at 184 K (warming) and 206 K (cooling).[12] Branch-chain and long-chain analogues of this type have also been reported, in a study aimed at producing bifunctional materials which display both liquid crystal and SCO features, with a primary aim of investigating the interrelated and/or synergistic effects of these properties.[13−16] Here, our focus has been directed toward a fundamental understanding of the structural, magnetic, and detailed EPR spectral properties of such Co(II)terpyRX chelates using comparison to the parent Co(II)terpy and terpyridone complexes to further elucidate the role that the various length alkyl chain groups has on SCO properties.

Experimental Section

General Information. All chemicals were used without further purification, solvents were dried and stored over molecular sieves, and the syntheses were carried out by use of syringe techniques, in an inert atmosphere of N_2, unless otherwise stated. The ligands were all synthesized by a slightly modified version of the method previously described by Andres et al.,[17] whereby 4′-hydroxy-2,2′:6′,2″-terpyridine (terpyOH) was used to react with the appropriate alkyl halide instead of the reported 4′-chloro-2,2′:6′,2″-terpyridine.

4″-Octoxy-2,2′:6′,2″-terpyridine (terpyR8). To a solution of 1.0 g (4 mmol) of 4′-hydroxo-2,2′:6′,2″-terpyridine in dry acetonitrile was added 1.55 g (8 mmol) of 1-bromooctane and dry potassium carbonate (0.56 g) upon which the solution turned from colorless to a pale yellowish color. After refluxing for 18 h the solution was cooled slowly to room temperature which caused the product to precipitate. The solvent was evaporated, and the product was washed with cold water and afterwards cold acetonitrile and left to dry in air yielding the ligand terpyR8 and an irremovable amount of KBr. Yield 1.155 g, 79.6%, as an off-white powder. Found: C, 59.26; H, 6.44; N, 9.04. $C_{12.42}H_{14.58}Br_{0.46}K_{0.46}N_{1.62}O_{0.54}$ (**terpyR8·0.85KBr**) requires C, 59.68; H, 5.88; N, 9.08%. ν_{max}(Nujol)/cm^{-1} 2922 (s, CH), 2856 (s, CH), 1583 (conj. CH), 1563 (conj. CH), 1461 (s, br, conj. CH, CH_2/CH_3), 1378 (CH_3), 1202 (C−O−C), 795, 744; δ_H (300 MHz; $CDCl_3$; Me_4Si) 0.91 (3 H, t, J = 6.9, CH_2CH_3), 1.33 (8 H, multiplet, $CH_2(CH_2)_4CH_3$), 1.52 (2 H, quintet, J=7.8, $CH_2CH_2(CH_2)_4$), 1.87 (2 H, quintet, J = 7.8, $OCH_2CH_2CH_2$), 4.24 (2 H, t, J=6.3, OCH_2CH_2), 7.34 (1 H, ddd, J=7.4, 4.9, and 1.2), 7.86 (1 H, td, J=7.5 and 1.7), 8.03 (1 H, s), 8.63 (1 H, dt, J= 8.1 and 1.0), 8.71 (1 H, ddd, J=4.7, 1.7, and 0.8); δ_C (300 MHz; $CDCl_3$; Me_4Si) 14.1, 22.7, 25.9, 29.0, 29.2, 29.3, 31.8, 68.2, 107.4, 121.3, 123.7, 136.8, 149.0, 156.2, 157.0, 167.4. m/z (EI MS) 361 (42, M^+), 332 (10, $M^+(CH_2CH_3)$), 318 (21, $M^+(CH_2)_2CH_3$), 304 (19, $M^+(CH_2)_3CH_3$), 262 (51, $M^+(CH_2)_6CH_3$), 249 (100, $M^+(CH_2)_7CH_3$). Crystals suitable for X-ray diffraction studies were obtained by slow evaporation.

4′-Butoxy-2,2′:6′,2″-terpyridine (terpyR4). The ligand terpyR4 was synthesized in a similar manner to the R8 ligand but replacing 1-bromooctane with 1-iodobutane. Yield of terpyR4 0.476 g, 38.9%; off-white powder; m/z (EI MS) 305 (M^+), 262 ($M^+(CH_2)_2CH_3$), 249 ($M^+(CH_2)_3CH_3$).

4′-Dodecoxy-2,2′:6′,2″-terpyridine (terpyR12). This ligand was also synthesized in the same way as the terpyR8 ligand but with 1-iodododecane replacing 1-bromooctane. Yield of terpyR12 0.796 g, 47.5%; off-white powder; m/z (EI MS) 417 (M^+), 374 ($M^+(CH_2)_2CH_3$), 304 ($M^+(CH_2)_7CH_3$), 262 ($M^+(CH_2)_{10}CH_3$), 249 ($M^+(CH_2)_{11}CH_3$).

$[Co(terpyR4)_2](BF_4)_2 \cdot H_2O$, $R4(BF_4) \cdot H_2O$. To a solution of terpyR4 (45.5 mg, 0.1 mmol) in a mixture of 6 mL of methanol and 4 mL of chloroform was added a methanolic solution of $Co(BF_4)_2 \cdot 6H_2O$ (30 mg, 0.05 mmol). The solution immediately changed from colorless to dark brown. Upon evaporation of the solvent, the product **$R4(BF_4) \cdot H_2O$** precipitated (55 mg, 87.5.5%), and it was washed with cold methanol. Found C, 52.88; H, 4.71; N, 9.52. $C_{38}H_{40}B_2CoF_8N_6O_3$ requires C, 53.55; H, 4.61; N, 9.86%. ν_{max}(KBr)/cm^{-1} 3421 (s, br, OH), 3090 (m, CH), 2958 (m, CH), 2863 (m, CH), 1617 (s, conj. CH), 1557

(5) Baker, W. A.; Judge, J. S. *Inorg. Chim. Acta* **1967**, *1*, 68–72.
(6) Kremer, S.; Henke, W.; Reinen, D. *Inorg. Chem.* **1982**, *21*, 3013–3022.
(7) Harris, C. M.; Lockyer, T. N.; Martin, R. L.; Patil, H. R. H.; Sinn, E.; Stewart, I. M. *Aust. J. Chem.* **1969**, *22*, 2105–2116.
(8) Brey, W. S.; Schmidt, J. G.; Stoufer, R. C. *Inorg. Chem.* **1967**, *6*, 268–271.
(9) Figgis, B. N.; Kucharski, E. S.; White, A. H. W. *Aust. J. Chem.* **1983**, *36*, 1527–1535.
(10) Galet, A.; Gaspar, A. B.; Muñoz, M. C.; Real, J. A. *Inorg. Chem.* **2006**, *45*, 4413–4422.
(11) Zhang, W.; Zhao, F.; Liu, T.; Yuan, M.; Wang, Z.M.; Gao, S. *Inorg. Chem.* **2007**, *46*, 2541–2555.
(12) Hayami, S.; Shigeyoshi, Y.; Akita, M.; Inoue, K.; Kato, K.; Osaka, K.; Takata, M.; Kawajiri, R.; Mitani, T.; Maeda, Y. *Angew. Chem., Int. Ed.* **2005**, *44*, 4899–4903. Hayami, S.; Murata, K.; Urakami, D.; Kojima, Y.; Akita, M.; Inoue, K. *Chem. Commun.* **2008**, 6510–6512.
(13) Hayami, S.; Moriyama, R.; Shuto, A.; Maeda, Y.; Ohta, K.; Inoue, K. *Inorg. Chem.* **2007**, *46*, 7692–7694.
(14) Hayami, S.; Motokawa, N.; Shuto, A.; Masuhara, N.; Someya, T.; Ogawa, Y.; Inoue, K.; Maeda, Y. *Inorg. Chem.* **2007**, *46*, 1789–1794.
(15) Gaspar, A. B.; Ksenofontov, V.; Seredyuk, M.; Gütlich, P. *Coord. Chem. Rev.* **2005**, *249*, 2661–2676.
(16) Seredyuk, M.; Gaspar, A. B.; Ksenofontov, V.; Reiman, S.; Galyametdinov, Y.; Haase, W.; Rentschler, E.; Gütlich, P. *Chem. Mater.* **2006**, *18*, 2513–2519.
(17) Andres, P. R.; Lunkwitz, R.; Pabst, G. R.; Böhn, K.; Wouters, D.; Schmatloch, S.; Schubert, U. S. *Eur. J. Org. Chem.* **2003**, *19*, 3769–3776.

(m, conj. CH), 1473 (s, conj. CH), 1440 (m, CH_2/CH_3), 1366 (m, CH_3), 1224 (s, $C_{conj}-OC$), 1058 (s, br, BF_4^-); *m/z* (ESI MS) 334.7 ($[Co(terpyR4)_2]^{2+}$), 756.1 ($[Co(terpyR4)_2]BF_4^+$).

$[Co(terpyR8)_2](BF_4)_2\cdot H_2O$, R8$(BF_4)\cdot H_2O$. As for **R4$(BF_4)\cdot H_2O$** but with 37 mg (0.1 mmol) of terpyR8 and 18 mg (0.09 mmol) of $Co(BF_4)_2\cdot 6H_2O$. Yield of orange brown product 61 mg, 91.5%. Found C, 56.86; H, 5.42; N, 8.69. $C_{46}H_{54}B_2CoF_8N_6O_3$ requires C, 56.75; H, 5.80; N, 8.63%. ν_{max}(KBr)/cm^{-1} 3453 (s, OH), 3093 (w, CH), 2925 (m, CH), 2853 (m, CH), 1616 (s, conj. CH), 1569 (m, conj. CH), 1556 (m, conj. CH), 1471 (s, conj. CH), 1439 (s, CH_2/CH_3), 1365 (s, CH_3), 1224 (m, $C_{conj}-O-C$), 1060 (s, br, BF_4^-); *m/z* (ESI MS) 390.7 ($[Co(terpyR8)_2]^{2+}$), 868.3 ($[Co(terpyR8)_2]BF_4^+$). Crystals of $[Co(terpyR8)_2](BF_4)_2\cdot H_2O$ were obtained by slow evaporation of the mother liquor.

$[Co(terpyR12)_2](BF_4)_2\cdot 8.5H_2O$, R12$(BF_4)\cdot 8.5H_2O$. As for **R4$(BF_4)\cdot H_2O$** but with 43 mg (0.1 mmol) of terpyR12 and 22 mg (0.065 mmol) of $Co(BF_4)_2\cdot 6H_2O$. Yield of orange-brown product 30 mg, 54.6%. Found C, 52.96; H, 6.15; N, 6.79 $C_{54}H_{87}B_2CoF_8N_6O_{10.5}$ requires C, 53.13; H, 7.18; N, 6.88%. ν_{max}(KBr)/cm^{-1} 3478 (s, br, OH), 3091 (m, CH), 2922 (s, CH), 2852 (s, CH), 1617 (s, conj. CH), 1557 (m, conj. CH), 1470 (s, conj. CH), 1439 (m, CH_2/CH_3), 1384 (m, CH_3), 1225 (m, $C_{conj}-O-C$), 1063 (s, br, BF_4^-); *m/z* (ESI MS) 446.8 ($[Co(terpyR12)_2]^{2+}$), 980.4 ($[Co(terpyR12)_2]BF_4^+$).

$[Co(terpyR4)_2](ClO_4)_2\cdot 1.5H_2O$, R4$(ClO_4)\cdot 1.5H_2O$. A methanolic solution of $Co(ClO_4)_2\cdot 6H_2O$ (28 mg, 0.765 mmol) was added to a solution of terpyR4 (45 mg, 0.15 mmol) in a mixture of 6 mL of methanol and 4 mL of chloroform. The solution immediately changed from colorless to a dark brown. Upon evaporation of the solvent the product was deposited, filtered, and washed with cold methanol. Orange-brown product. Yield 56 mg, 87.5%. Found C, 50.65; H, 4.22; N, 9.14. $C_{38}H_{39.5}Cl_2CoN_6O_{11.5}$ requires C, 50.96; H, 4.61; N, 9.38%. *m/z* (ESI MS) 334.7 ($[Co(terpyR4)_2]^{2+}$), 768.1 ($[Co(terpyR4)_2]ClO_4^+$). ***Safety warning!*** *Perchlorate salts of complexes containing organic ligands are potentially explosive, so great care should be exercised in using tiny quantities and not heating or grinding solid materials.*

$[Co(terpyR8)_2](ClO_4)_2$, R8(ClO_4). As for **R4(ClO_4)** but using terpyR8 (54 mg, 0.147 mmol) and $Co(ClO_4)_2\cdot 6H_2O$ (28 mg, 0.79 mmol). Crystals for X-ray diffraction studies were obtained by slow evaporation. Yield 61 mg, 91.5%. Found C, 54.09; H, 5.60; N, 8.07. $C_{46}H_{54}Cl_2CoN_6O_{10}$ requires C, 56.33; H, 5.55; N, 8.75%. *m/z*(ESI MS) 390.7 ($[Co(terpyR8)_2]^{2+}$), *m/z* 880.3 ($[Co(terpyR8)_2]ClO_4^+$).

$[Co(terpyR12)_2](ClO_4)_2\cdot 7.5H_2O$, R12$(ClO_4)\cdot 7.5H_2O$. As for **R4$(ClO_4)$** but using terpyR12 (42 mg, 0.1 mmol) and $Co(ClO_4)_2\cdot 6H_2O$ (21 mg, 0.57 mmol). Orange-brown product. Yield 45 mg, 81.9%. Found C, 52.66; H, 5.93; N, 6.33. $C_{54}H_{85}Cl_2CoN_6O_{17.5}$ requires C, 52.81; H, 6.98; N, 6.84%. *m/z*(ESI MS) 446.8 ($[Co(terpyR12)_2]^{2+}$), 992.3 ($[Co(terpyR12)_2]ClO_4^+$).

$[Co(terpyR4)_2](PF_6)_2\cdot 3H_2O$, R4$(PF_6)\cdot 3H_2O$. To a methanolic solution of terpyR4 (46.5 mg, 0.10 mmol) was added a solution of $CoCl_2\cdot 6H_2O$ (19 mg, 0.054 mmol) in methanol. A solution of KPF_6 (22 mg, 0.12 mmol) in water was then added to the resulting dark orange-brown solution. The volume was reduced followed by cooling on ice to yield the product. Yield 62 mg, 84.9%. Found C, 45.35; H, 4.07; N, 7.94. $C_{38}H_{44}CoF_{12}N_6O_5P_2$ requires C, 45.03; H, 4.38; N, 8.29%. *m/z* (ESI MS) 334.7 ($[Co(terpyR4)_2]^{2+}$), 814.1 ($[Co(terpyR4)_2]PF_6^+$). Single crystals were obtained by slow crystallization from the preparative solution.

$[Co(terpyR8)_2](PF_6)_2\cdot 5H_2O$, R8$(PF_6)\cdot 5H_2O$. As for **R4 $(PF_6)\cdot 5H_2O$** but using terpyR8 (37 mg, 0.10 mmol), $CoCl_2\cdot 6H_2O$ (11 mg, 0.054 mmol), and KPF_6 (22 mg, 0.12 mmol). Yield 53 mg, 96.6%. Found C, 47.89; H, 4.85; N, 7.15. $C_{46}H_{64}CoF_{12}N_6O_7P_2$ requires C, 47.55; H, 5.55; N, 7.23%. *m/z* (ESI MS) 390.8 ($[Co(terpyR8)_2]^{2+}$), 926.3 ($[Co(terpyR8)_2]PF_6^+$).

$[Co(terpyR12)_2](PF_6)_2\cdot CH_3OH$, R12$(PF_6)\cdot CH_3OH$. As for **R4$(PF_6)\cdot 5H_2O$** but with terpyR12 (42 mg, 0.1 mmol), $CoCl_2\cdot 6H_2O$ (14.5 mg, 0.06 mmol), and KPF_6 (22 mg, 0.12 mmol) used. Orange-brown product, yield 40 mg, 67.2%. Found C, 55.53; H, 6.23; N, 6.49. $C_{55}H_{74}CoF_{12}N_6O_3P_2$ requires C, 54.32; H, 6.13; N, 6.91%. *m/z* (ESI MS) 446.8 ($[Co(terpyR12)_2]^{2+}$), 1038.3 ($[Co(terpyR12)_2]PF_6^+$).

$[Co(terpyR4)_2](B(C_6H_5)_4)_2\cdot 20H_2O$, R4$(BPh_4)\cdot 20H_2O$. A solution of $CoCl_2\cdot 6H_2O$ (19 mg, 0.08 mmol) in methanol was added to a methanolic solution of terpyR4 (45 mg, 0.15 mmol), resulting in a clear brownorange solution. A methanolic solution of $NaB(C_6H_5)_4$ (55 mg, 0.16 mmol) was added which yielded an immediate precipitate. Orange-brown compound, yield 94 mg, 97.5%. Found C, 60.30; H, 4.73; N, 4.83. $C_{86}H_{118}B_2CoN_6O_{22}$ requires C, 61.91; H, 7.61; N, 5.04%. *m/z* (ESI MS) 334.7 ($[Co(terpyR4)_2]^{2+}$), 988.3 ($[Co(terpyR4)_2]B(C_6H_5)_4^+$).

$[Co(terpyR8)_2](B(C_6H_5)_4)_2\cdot 3H_2O$, R8$(BPh_4)\cdot 3H_2O$. As for **R4$(BPh_4)\cdot 3H_2O$** but with terpyR8 (36 mg, 0.10 mmol), $CoCl_2\cdot 6H_2O$ (12.5 mg, 0.062 mmol), and $NaB(C_6H_5)_4$ (43 mg, 0.12 mmol). Yield 64 mg, 90.5%. Found C, 76.92; H, 6.84; N, 5.64. $C_{94}H_{100}B_2CoN_6O_5$ requires C, 76.57; H, 6.84; N, 5.70%. *m/z* (ESI MS) 390.8 ($[Co(terpyR8)_2]^{2+}$), 1100.5 ($[Co(terpyR8)_2]B(C_6H_5)_4^+$).

$[Co(terpyR12)_2](B(C_6H_5)_4)_2\cdot 9H_2O$, R12$(BPh_4)\cdot 9H_2O$. As for **R4$(BPh_4)\cdot 3H_2O$** but with terpyR12 (45 mg, 0.1 mmol), $CoCl_2\cdot 6H_2O$ (14 mg, 0.057 mmol), and $NaB(C_6H_5)_4$ (35 mg, 0.1 mmol). Orange-brown product, yield 70 mg, 89.3%. Found C, 71.44; H, 6.29; N, 5.07. $C_{102}H_{128}B_2CoN_6O_{11}$ requires C, 72.29; H, 7.61; N, 4.96%. *m/z* (ESI MS) 446.8 ($[Co(terpyR12)_2]^{2+}$), 1212.5 ($[Co(terpyR12)_2]B(C_6H_5)_4^+$).

Physical Measurements. IR spectra were measured using an EQUINOX IFS 55 spectrometer with the samples prepared as KBr disks. ATR-IR were also preformed on an EQUINOX 55 fitted with an ATR device, and the Raman experiments were done at 633 nm on a Renishaw Ramascope RM200 equipped with a PULNIX TMC 312 color camera. ESI mass spectral (MS) measurements were performed using a Micromass Platform II with methanol as the solvent.

Magnetic Susceptibility Measurements. Measurements were made using a Quantum Design DC SQUID MPMS5 magnetometer with a DC field of 1 T. Samples were contained in gelatin capsules attached to the end of the sample rod. The instrument was calibrated against a standard palladium sample provided by Quantum Design and checked against the chemical calibrant, $CuSO_4\cdot 5H_2O$. To allow thermal equilibrium to occur in these SCO species, long times were taken at each temperature point and between points.

Crystallographic Data Collection and Refinement. Single crystal data for **terpyR8** were collected on a Bruker-Nonius X8APEXII CCD diffractometer equipped with graphitemonochromated Mo Kα radiation ($\lambda = 0.71073$ Å). Single crystal data for **R8(ClO_4)**, **R8$(BF_4)\cdot H_2O$**, and **R4$(PF_6)\cdot 3H_2O$** were collected on a Bruker APEX X8 diffractometer equipped with graphitemonochromated Mo Kα radiation ($\lambda = 0.7017$ Å) and an Oxford Instruments Nitrogen Cryostream (123(2) K). Single crystals were mounted on a MiTeGen MicroMounts fiber in a thin smear of oil. Diffraction data analysis and reduction were performed within SMART and SAINT+.[18] Correction for Lorenz, polarization, and absorption effects was performed within SADABS.[19] The structure was solved using a combination of direct and Patterson methods within SHELXS97 and refined using

(18) *SMART, SAINT, and XPREP: Area Detector control and data integration and reduction software*; Bruker Analytical X-ray Instruments Inc.: Madison, WI, 1995.

(19) Sheldrick, G. M. *SADABS: Empirical Absorption Corrections Program for Area Detector Data* University of Göttingen: Göttingen, Germany, 1996.

Table 1. Single Crystal X-ray Diffraction Data and Refinement Details for terpyR8, $[Co(terpyR8)_2](ClO_4)_2$, **R8(ClO$_4$)**, $[Co(terpyR4)_2](PF_6)_2 \cdot 3H_2O$, **R4(PF$_6$)·3H$_2$O**, and $[Co(terpyR8)_2](BF_4)_2 \cdot H_2O$, **R8(BF$_4$)·H$_2$O**

compound	terpyR8	$[Co(terpyR8)_2](ClO_4)_2$	$[Co(terpyR4)_2](PF_6)_2 \cdot 3H_2O$	$[Co(terpyR8)_2](BF_4)_2 \cdot H_2O$
formula	$C_{23}H_{27}N_3O$	$Co(C_{46}H_{54}N_6O_2)(ClO_4)_2$	$[CoC_{38}H_{38}N_6O_2](PF_6)_2 \cdot 3H_2O$	$[CoC_{46}H_{54}N_6O_2](BF_4)_2 \cdot H_2O$
T, K	180(2)	123(2)	123(2)	123(2)
FW, g mol^{-1}	361.48	980.78	965.54	971.50
crystal system (space group)	monoclinic ($P2/c$)	triclinic ($P\bar{1}$)	triclinic ($P\bar{1}$)	triclinic ($P\bar{1}$)
a, Å	18.570(3)	8.8129(3)	9.0420(3)	10.9642(4)
b, Å	5.4007(7)	13.3020(4)	12.4596(5)	11.9275(5)
c, Å	21.055(3)	20.2516(6)	16.0592(6)	19.5431(8)
α, deg	90.00	104.983(2)	83.039(2)	78.488(2)
β, deg	111.356(5)	94.245(2)	86.455(2)	89.505(2)
γ, deg	90.00	97.3500(10)	88.317(2)	86.303(2)
V, Å^3	1966.6(5)	2260.27(12)	1792.02(11)	2499.11(17)
ρ_{calcd}, Mg m^{-3}	1.221	1.441	1.789	1.291
μ, mm^{-1}	0.076	0.564	0.686	0.417
$R(F)$, % $\{I > 2\sigma(I)$, all$\}$	0.0497{0.1331}	0.1092{0.1229}	0.1286{0.1545}	0.1665{0.1748}
$R_w(F^2)$/% $\{I > 2\sigma(I)$, all$\}$	0.0966{0.1202}	0.2198{0.2259}	0.2895{0.3058}	0.4697{0.4836}
GOF	0.958	1.310	1.155	2.180
$R(F)$, % $\{I > 2\sigma(I)$, all$\}$squeezed				0.0650{0.0757}
$R_w(F^2)$, % $\{I > 2\sigma(I)$, all$\}$squeezed				0.1662{0.1727}
GOFsqueezed				1.085

SHELXL-97 within X-SEED.[20,21] CCDC-674131-33 and 699797 contain the crystal data for this paper. These data can be obtained free of charge via www.ccdc.cam.ac.uk/conts/retrieving.html (or from the Cambridge Crystallographic Data Centre, Union Road, Cambridge, CB21EZ, UK; fax: (+44)1223336033; or deposit@ccdc.cam.ac.uk). All non-hydrogen atoms in the structures were refined anisotropically, and hydrogen atoms were generated using the Riding model. A number of constraints and restraints were required for the structures **R8(BF$_4$)·H$_2$O** and **R4(PF$_6$)·3H$_2$O** for stable refinements; see Supporting Information for details. Structural refinement for **R8(BF$_4$)·H$_2$O** was carried out on both the original data set and that for which the data had been run through the SQUEEZE protocol within PLATON.[22] The latter resulted in a much improved refinement, and the refinement details are given in Table 1.

EPR Measurements. X-band (ca. 9.5 GHz) EPR spectra of polycrystalline powders and frozen solutions were recorded with a Bruker ESP380E CW/FT spectrometer. Using the standard rectangular TE_{012} cavity, sample temperatures between 295 and 105 K were reached using a Bruker VT 4111 temperature controller and associated nitrogen gas flow insert and a temperature of 77 K using a glass finger dewar. Temperatures between approximately 100 and 2.5 K were obtained with an Oxford Instruments CF935 continuous flow cryostat with the sample tube inserted in a ER4118 cylindrical cavity insert. Temperatures below 100 K were calibrated against a germanium thermometer using a carbon resistor as a transfer standard. Microwave frequencies were measured with an EIP Microwave 548A frequency counter, and the $g$factors were determined with reference to the F^+ line in CaO (2.0001 ± 0.0001).[23] The spectra were obtained at microwave powers well below saturation levels, with typical spectrometer settings being gain 5×10^4, 100 kHz modulation amplitudes of 1.0 −5.0 G, scan ranges of 1200−2000 G in 82 s, and time constants of 20.5−81.9 ms. Spectrum simulations were performed with the XSophe-Sophe-XeprView computer simulation software suite described by Hanson et al.[24]

Comparisons of spectral intensities were performed by double integration of the first derivative spectra as obtained experimentally using the integration program included in the Bruker WINEPR software suite. Because of the different experimental arrangements, the comparisons for a given sample needed to be divided into two temperature ranges, namely, 2.5 K to approximately 80 K (cylindrical cavity, liquid helium cryogen) and 110 to 250 K (rectangular cavity, liquid nitrogen cryogen). The comparisons within a given temperature range assume that the cavity Q factor remains unchanged and rely on the accuracy of the temperature measurement and the uniformity of the temperature over the sample volume.[25]

The multifrequency (Q-, X-, S-band) EPR spectra were recorded with Bruker Elexsys E500 and E580 CW EPR spectrometers. A cylindrical TE_{011} cavity, a super high Q-cavity, and a flexline resonator were employed for Q-, X-, S-band measurements, respectively. For low temperature X-band measurements, an Oxford Instruments ESR910 cryostat in conjunction with an ITC 503 temperature controller was employed to achieve temperatures between approximately 100 K and 1.5 K. For the Q and S-band measurements a flow through CF935LT cryostat replaced the ESR910 cryostat used at X-band frequencies. Microwave frequencies and the magnetic field were calibrated with an EIP Microwave 548B (Elexsys E500) and Bruker (Elexsys E580) frequency counters and Bruker ER036 M teslameters for both instruments. Spectral simulations were performed with the XSophe-Sophe-XeprView computer simulation software suite described by Hanson et al.[24] in conjunction with octave (www.gnu.org/software/octave/) to simultaneously optimise the spin Hamiltonian parameters to the S-, X- and Q-band spectra. Computer simulations were performed on a Linux cluster running Mandriva 2007 as the operating system.

Results and Discussion

Synthesis. Orange-brown powders of the analogous Co(II) complexes with the general formula $[Co(terpyRX)_2](Y)_2 \cdot nH_2O$ were all readily synthesized by mixing methanol/chloroform solutions of the appropriate RX ligand,[17] with methanolic solutions of $Co(Y)_2 \cdot 6H_2O$, $Y = ClO_4^-$, BF_4^-. The PF_6^- and BPh_4^- salts were made

(20) Sheldrick, G. M. *SHELXS-97: Program for crystal structure solution*; University of Göttingen: Göttingen, Germany, 1997.
(21) Barbour, L. J. *X-SEED*; University of Stellenbosch; Stellenbosch, South Africa, 1999.
(22) Spek, A. L. *PLATON, A Multipurpose Crystallography Tool*; Utrecht University: Utrecht, The Netherlands, 2000.
(23) Wertz, J. E.; Orton, J. W.; Auzins, P. *Disc. Faraday Soc.* **1961**, *31*, 140–150.
(24) Hanson, G. R.; Gates, K. E.; Noble, C. J.; Griffin, M.; Mitchell, A.; Benson, S. *J. Inorg. Biochem.* **2004**, *98*, 903–916.
(25) Strictly speaking, this analysis needs to be performed in frequency space. However, where g is close to isotropic and the shape of the spectrum is not changed substantially, the errors introduced by performing double integration in field space (as in the present case) will not be significant. See ref 31, pp 42−53.

Table 2. Selected Co-N Bond Lengths and N-Co-N Angles for $[Co(terpyR8)_2]\cdot(ClO_4)_2$, **R8(ClO4)**, $[Co(terpyR8)_2](BF_4)_2\cdot H_2O$, **R8(BF4)·H2O**, and $[Co(terpyR4)_2](PF_6)_2\cdot 3H_2O$, **R4(PF6)·3H2O**, at 123 K

$[Co(terpyR8)_2](ClO_4)_2$							
Co-N (Å)		*cis*-N-Co-N (deg)		*cis*-N-Co-N (deg)		*trans*-N-Co-N (deg)	
Co(1)-N(1)	2.176(3)	N(1)-Co(1)-N(6)	92.00(13)	N(3)-Co(1)-N(4)	90.53(13)	N(6)-Co(1)-N(4)	161.72(13)
Co(1)-N(2)	1.918(3)	N(1)-Co(1)-N(4)	94.28(13)	N(3)-Co(1)-N(6)	90.31(13)	N(1)-Co(1)-N(3)	157.16(12)
Co(1)-N(3)	2.136(3)	N(2)-Co(1)-N(1)	78.49(13)	N(5)-Co(1)-N(1)	102.48(13)	N(2)-Co(1)-N(5)	178.97(14)
Co(1)-N(4)	2.012(3)	N(2)-Co(1)-N(3)	78.70(13)	N(5)-Co(1)-N(3)	100.32(13)		
Co(1)-N(5)	1.865(3)	N(2)-Co(1)-N(4)	99.43(13)	N(5)-Co(1)-N(4)	80.88(13)		
Co(1)-N(6)	1.997(3)	N(2)-Co(1)-N(6)	98.64(13)	N(5)-Co(1)-N(6)	81.00(13)		
$[Co(terpyR8)_2](BF_4)_2\cdot H_2O$							
Co-N (Å)		*cis*-N-Co-N (deg)		*cis*-N-Co-N (deg)		*trans*-N-Co-N (deg)	
Co(1)-N(1)	1.953(6)	N(1)-Co(1)-N(6)	90.3(2)	N(3)-Co(1)-N(4)	91.4(3)	N(6)-Co(1)-N(4)	164.7(3)
Co(1)-N(2)	1.861(7)	N(1)-Co(1)-N(4)	90.7(2)	N(3)-Co(1)-N(6)	91.8(3)	N(1)-Co(1)-N(3)	164.5(3)
Co(1)-N(3)	1.940(6)	N(2)-Co(1)-N(1)	82.3(2)	N(5)-Co(1)-N(1)	97.3(2)	N(2)-Co(1)-N(5)	179.6(2)
Co(1)-N(4)	1.940(7)	N(2)-Co(1)-N(3)	82.2(3)	N(5)-Co(1)-N(3)	98.2(3)		
Co(1)-N(5)	1.871(6)	N(2)-Co(1)-N(4)	97.5(3)	N(5)-Co(1)-N(4)	82.5(3)		
Co(1)-N(6)	1.945(6)	N(2)-Co(1)-N(6)	97.7(3)	N(5)-Co(1)-N(6)	82.3(3)		
$[Co(terpyR4)_2](PF_6)_2\cdot 3H_2O$							
Co-N (Å)		*cis*-N-Co-N (deg)		*cis*-N-Co-N (deg)		*trans*-N-Co-N (deg)	
Co(1)-N(1)	1.928(5)	N(1)-Co(1)-N(6)	91.64(19)	N(3)-Co(1)-N(4)	91.3(2)	N(6)-Co(1)-N(4)	164.35(16)
Co(1)-N(2)	1.855(5)	N(1)-Co(1)-N(4)	89.4(2)	N(3)-Co(1)-N(6)	91.93(19)	N(1)-Co(1)-N(3)	164.2(2)
Co(1)-N(3)	1.942(5)	N(2)-Co(1)-N(1)	82.4(2)	N(5)-Co(1)-N(1)	96.81(18)	N(2)-Co(1)-N(5)	179.00(18)
Co(1)-N(4)	1.936(5)	N(2)-Co(1)-N(3)	81.9(2)	N(5)-Co(1)-N(3)	98.90(17)		
Co(1)-N(5)	1.864(3)	N(2)-Co(1)-N(4)	98.6(2)	N(5)-Co(1)-N(4)	82.07(17)		
Co(1)-N(6)	1.943(4)	N(2)-Co(1)-N(6)	97.05(17)	N(5)-Co(1)-N(6)	82.30(13)		

by metathesis starting from $CoCl_2\cdot 6H_2O$. Using numbering as follows; $Co(terpyR4)_2$ as **R4**, $Co(terpyR8)_2$ as **R8**, $Co(terpyR12)_2$ as **R12**, the families of compounds are labeled according to the anion and degree of solvation, **R4(ClO4)·1.5H2O**, **R4(BF4)·H2O**, **R4(PF6)·3H2O**, **R4(BPh4)·20H2O**, **R8(ClO4)**, **R8(BF4)·H2O**, **R8(PF6)·5H2O**, **R8(BPh4)·3H2O**, **R12(ClO4)·7.5H2O**, **R12(BF4)·8.5H2O**, **R12(PF6)·CH3OH**, and **R12(BPh4)·9H2O**. The nature and degree of solvation was obtained from microanalytical data and single crystal data where available.

ESI mass spectral measurements on methanol solutions and ATR-IR and Raman spectral measurements on powders (Supporting Information, Table S5) were used to characterize the Co(II) products. Since the differences in the ligands are in the varying chain length, it was hoped that minor differences would show up in the IR region of the sp^3 C−H stretching frequencies. Within the free ligand and the Co chelate spectra, using both ATR and Raman methods, there was a slight tendency toward increased intensity of these vibrational peaks as the chain length increased from R4 to R12.

Single Crystal X-ray Diffraction. Single crystal X-ray diffraction structural analysis and refinement details of all materials are reported in Table 1, and selected bond lengths and angles are reported in Table 2. Other relevant data are included in the Supporting Information.

Structure of the Free Ligand terpyR8. The molecular structure and crystal packing of the free ligand was carried out to compare with the structures of the cobalt(II)−terpyR8 complexes. The free ligand crystallizes where the pyridyl nitrogen atoms are disposed as far apart as possible, such that rotation of the outer pyridine rings must occur to yield the characteristic meridional form upon metal chelation. The $O(CH_2)_7CH_3$ (R8) chain is crystallographically ordered and has a "straight" conformation. The packing of the free ligands in each unit cell (where there are four R8 molecules per unit cell) is dominated by parallel packed "columns" of ligands aligned in the same direction, that is, head-to-head and tail-to-tail (Figures S1 and S2 and Table S1, Supporting Information). Within these columns, adjacent ligands are involved in C(H)···π (2.790(3) Å) and $\pi\cdots\pi$ (3.373(3) Å) interactions (Figure S4, Supporting Information). The columns of ligands occur in "pairs" within the unit cell such that the hydrophobic alkyl chains are parallel and the terpy groups face outward (Figure S3, Supporting Information).

Structure of [Co(terpyR8)2](ClO4)2, R8(ClO4). Single crystal analysis of the orange crystals of **R8(ClO4)** revealed a mononuclear complex of the formula $[Co(terpyR8)_2](ClO_4)_2$ (Table 1). The asymmetric unit contains one cobalt(II) atom in a compressed octahedral environment comprised of two terpyR8 ligands in a *bis*-tridentate meridional fashion bound through the terpy end of the ligand (Figure 2 and Table 2). The average Co−N bond length is 2.017(3) Å, where notably the central Co−N-(pyridine) distances are shorter (av. 1.891(3) Å) than the outer ones (av. 2.080(3) Å), as is characteristic in this type of compound. Furthermore, it is interesting to note that the two terpy moieties are not at equal distance from the Co(II) ion; the terpy unit containing N(1)N(2)N(3) is further away than the other (Figure 2). Comparison of bond lengths from the previously reported parent complex ion, $[Co(terpy)_2]^{2+}$,[9,26,27] shows average values of approximately 2.05 Å at 295 K and approximately

(26) Figgis, B. N.; Kucharski, E. S.; White, A. H. W. *Aust. J. Chem.* **1983**, *36*, 1537–1561.
(27) Henke, W.; Kremer, S. *Inorg. Chim. Acta* **1982**, *65*, L115–L117.

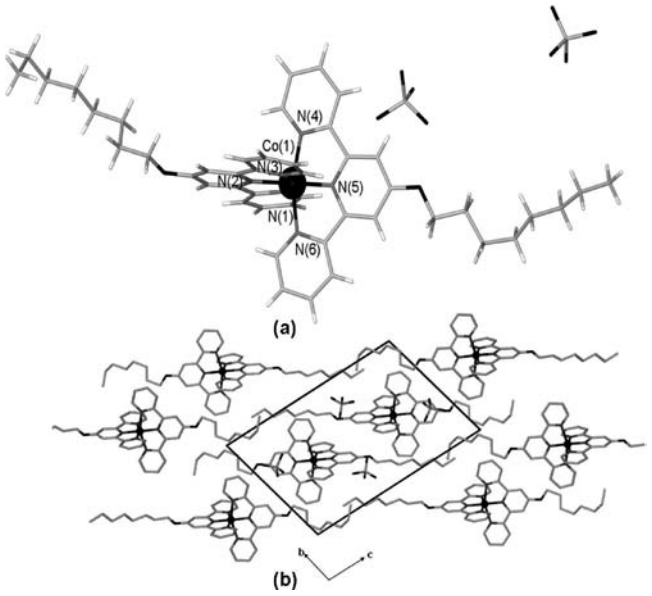

Figure 2. (a) Structure of $[Co(terpyR8)_2](ClO_4)_2$, **R8(ClO$_4$)**. (b) Crystal packing of **R8(ClO$_4$)**; the hydrogen atoms have been omitted for clarity.

2.03 Å at 120 K (iodide salt),[9] which is a very small change across the HS → LS spin transition compared to the approximately 0.2 Å change commonly found in Fe(II) systems.[1−4] Unlike complex **R8(ClO$_4$)**, these $[Co(terpy)_2]^{2+}$ complexes did not show one terpy unit to be more closely bound than the other. Similar tendencies to those in **R8(ClO$_4$)** were also found for the terpyridone Co(II) compounds with a change in spin being accompanied by a small change in bond length and with the Co−N(pyridone) length being the shortest (av. 1.920 Å at 293 K and av. 1.907 Å at 105 K for the BF_4/SiF_6(0.5) salt).[10] In this case, there was evidence for one terpyOH ligand being bound slightly more closely than the other, and this varied with the anion and the solvent molecules present.

The C_8 alkyl chain portion of the coordinated ligand in **R8(ClO$_4$)** is ordered but is not a regular straight alkyl chain as was the case in the free ligand crystal structure. Here, the chains adopt a slightly bent shape, one being more bent than the other, such that they are oriented on the same side of the Co(II) ion, in a related but not identical way to that observed in the analogous C_{16} compound.[12] Furthermore, associated with each mononuclear species are two perchlorate anions where their oxygen atoms are all involved in C(H)···O interactions with both the terpy aromatic groups and alkyl chains on the neighboring mononuclear moieties (Table S2, Supporting Information). As such, this material contains an extensive network of hydrogen bonds. Surprisingly, considering the large number of aromatic rings and the close packed nature of the material, there are no $\pi-\pi$ interactions between the $[Co(terpyR8)_2]^{2+}$ species in the crystal lattice. A similar lack of intermolecular $\pi-\pi$ interactions was noted in the $Co(terpyOH)_2^{2+}$ family that showed rather similar spin crossover magnetic plots to that of **R8(ClO$_4$)**.[10] This contrasts with the packing noted in the free ligand and in $[Co(terpyRX)_2](BF_4)_2$, X = 14 and 16,[12] as well as in a family of $[Fe^{II}$(2-tetrazole-2-RX-5-yl)-1,10-phenanthroline$)_2]^{2+}$ (X = 1−8, 10, 12, 14, 16) compounds[11] in which the lateral pyridine rings formed sheets via $\pi-\pi$ interactions. The spin transitions and cooperativity in these Co(II) and Fe(II) materials were influenced by such $\pi-\pi$ interactions, when combined with other intermolecular effects.[11,12] Finally, the mononuclear moieties in **R8(ClO$_4$)** are close packed such that there is no solvent included in the crystal lattice (Figure 2).

Structure of $[Co(terpyR8)_2](BF_4)_2\cdot H_2O$, R8$(BF_4)\cdot H_2O$. Variation of anion with the terpyR8 ligand to BF_4^- resulted in essentially the same mononuclear unit as for **R8(ClO$_4$)**; however, the crystal packing is different, as evidenced by the different unit cell axes and volume. The structure consists of a cobalt(II) atom in a compressed octahedral environment, whereby each cobalt(II) is surrounded by two terpyR8 ligands in a *bis*-tridentate fashion through the terpy end of the ligand. The average Co−N bond length is 1.915(3) Å (Table 2). While this is lower than the value observed for **R8(ClO$_4$)**, such values have been noted for LS forms of **R14$(BF_4)\cdot$MeOH**[12] and of the $[Co(terpyOH)_2]^{2+}$ compounds.[10] One alkyl chain is completely regular, as observed for **R8(ClO$_4$)**; however, the other one is disordered at carbon positions 2 and 6 (Figure 3). Interestingly, the ordered chain is involved in significantly more hydrogen bonding interactions with the BF_4^- anions than is the disordered chain (Supporting Information, Table S3, Figure S5). There are two BF_4^- anions associated with each mononuclear species; one is completely ordered, and all the fluorine atoms are involved in hydrogen bonding interactions with the aromatic rings from the $[Co(terpyR8)_2]^{2+}$ moiety (Supporting Information, Figure S5). The remaining BF_4^- anion is disordered over three crystallographically distinct sites (Supporting Information, Figure S5). These anions each hydrogen bond with the one water molecule (this is different to **R8(ClO$_4$)** which had no solvent included) and to varying extents with the $[Co(terpyR8)_2]^{2+}$ species, in particular with the ordered alkyl chain (Supporting Information, Figure S5). As observed for **R8(ClO$_4$)**, there are no $\pi-\pi$ interactions between the $[Co(terpyR8)_2]^{2+}$ species in the crystal lattice.

Structure of $[Co(terpyR4)_2](PF_6)_2\cdot 3H_2O$, R4$(PF_6)\cdot 3H_2O$. Single crystal analysis of well formed orange crystals revealed a mononuclear complex of the formula $[Co(terpyR4)_2](PF_6)_2\cdot 3H_2O$ (Table 1). The structure was solved in the triclinic space group $P\bar{1}$, and the asymmetric unit contains one cobalt(II) atom in a compressed octahedral environment. Each cobalt(II) is surrounded by two terpyR4 ligands in a *bis*-tridentate fashion through the terpy end of the ligand. The average Co−N bond length of 1.911(3) Å, at 123 K, is shorter than in **R8(ClO$_4$)** and **R8$(BF_4)\cdot H_2O$** (Figure 4, Table 2) and is indicative of LS Co(II), as confirmed by magnetic data. The bonds to the central pyridine units in the terpyR4 moieties are, as observed in the other analogues, the shortest (av. 1.859 (5) Å); however, the two ligands show more equal Co−N distances than was the case in **R8(ClO$_4$)**. The entire alkyl chain portions of each ligand were not located in the difference map, presumably due to severe disorder/diffuse scattering/motion of the chains; one ligand is missing one carbon and the other is missing two. However, both mass spectroscopy and CHN analysis confirm the presence of the entire R4 ligand in the bulk polycrystalline

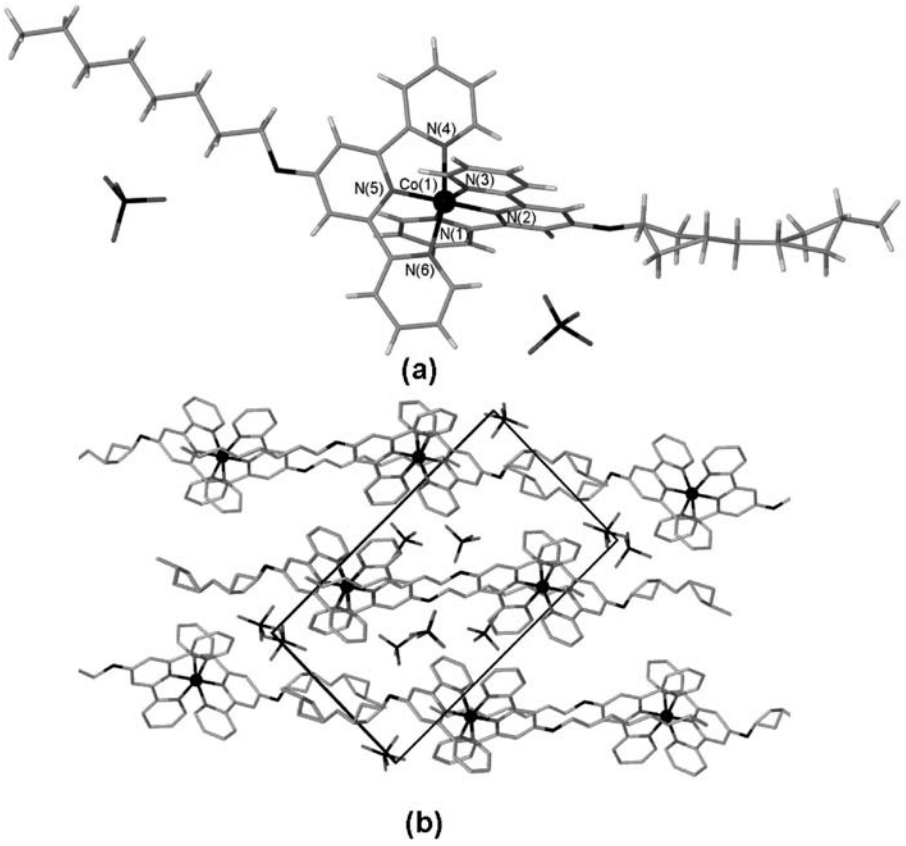

Figure 3. (a) Structure of $[Co(terpyR8)_2](BF_4)_2 \cdot (H_2O)$, **R8(BF$_4$)·H$_2$O**, showing the disorder on one alkyl chain. (b) Crystal packing of **R8(BF$_4$)·H$_2$O**, the hydrogen atoms, and disordered BF_4^- have been omitted for clarity.

sample. The possibility that any of these three $[Co(terpyRX)_2]^{2+}$ compounds contain significant or trace amounts of the Co(III) analogue can be ruled out in view of the microanalytical and magnetic data as well as comparison of Co−N bond lengths to published, related Co(II) species.[10,12]

Within the crystal lattice, the mononuclear moieties of the R4 complex are close packed; however, there are three water molecules and two PF_6^- anions associated with each mononuclear complex. One of the PF_6^- anions has all of the fluorine atoms disordered over two sites; all of these atoms are involved in hydrogen bonding interactions. Interestingly, the other PF_6^- anion has only two of its fluorine atoms disordered over two sites, and only these two are involved in hydrogen bonding interactions (Supporting Information, Table S4 and Figure S6). These interactions occur between the PF_6^- anions and solvent water molecules or aromatic C(H) groups. Again, there are no $\pi-\pi$ interactions present between the $[Co(terpyR4)_2]^{2+}$ species in the crystal lattice.

Magnetic Properties. Magnetic susceptibility measurements were carried out on 12 powder samples (three alkyl chain lengths and four anions) and relevant, representative plots of the three BF_4^- compounds that were investigated by EPR spectroscopy, namely, **R4(BF$_4$)·H$_2$O**, **R8(BF$_4$)·H$_2$O**, and **R12(BF$_4$)·8.5H$_2$O**, are shown in Figure 5. The susceptibility plots for all other materials are located in the Supporting Information, Figures S12−S20. In general, these complexes exhibit gradual, incomplete spin transitions, from $S = 1/2$ to $S = 3/2$, with increasing temperature, a common feature in cobalt(II) spin crossover systems.[5−10,12] Between 4 and 150 K, the shortest chain analogue **R4(BF$_4$)·H$_2$O** displays minimum $\chi_M T$ values of 0.38 cm^3 K mol^{-1} which is indicative of a complete LS character. Above 150 K, the $\chi_M T$ values increase gradually to reach a maximum $\chi_M T$ value of 1.80 cm^3 K mol^{-1} at 350 K, suggesting the transition to the HS state is not complete even at high temperatures. Thus the spin transition for **R4(BF$_4$)·H$_2$O** spans a large temperature range of approximately 200 K and has a characteristic $T_{1/2}$ value of approximately 270 K. No thermal hysteresis in the heating and cooling modes was observed.

The intermediate chain length analogue **R8(BF$_4$)·H$_2$O** shows temperature dependent magnetic moment properties similar to **R4(BF$_4$)·H$_2$O**, such that there is a low temperature plateau of $\chi_M T = 0.45$ cm^3 K mol^{-1} indicative of complete LS character. Above 100 K, the $\chi_M T$ values gradually increase to a maximum value of approximately 2.13 cm^3 K mol^{-1} also indicative of an incomplete HS nature at high temperatures. The spin transition for this material occurs over a broader temperature range, that is, 100−350 K, than the R4 analogue and has slightly lower $T_{1/2}$ value of 235 K. Again, no thermal hysteresis in the $\chi_M T$ values was observed in the heating and cooling modes.

The magnetic moment temperature dependence of the longest chain analogue **R12(BF$_4$)·8.5H$_2$O** displays quite a different SCO nature than the shorter chain analogues but still shows a gradual incomplete nature. At high temperatures, in contrast to the other analogues, close to complete HS character is observed with a maximum

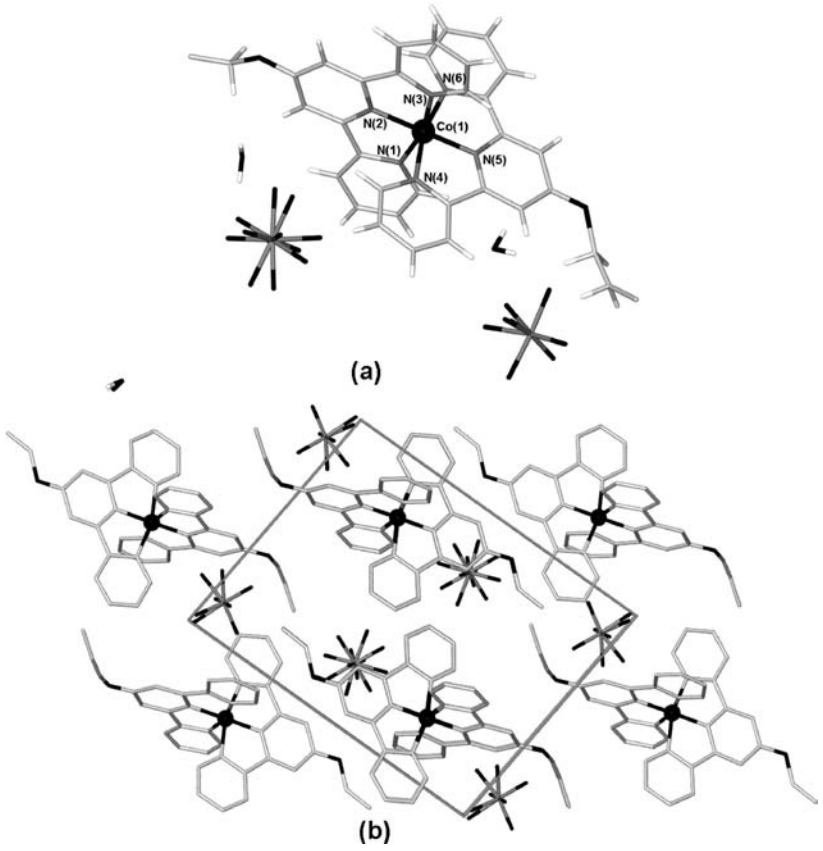

Figure 4. (a) Structure of $[Co(terpyR4)_2](PF_6)_2 \cdot 3H_2O$, **R4(PF$_6$)·3H$_2$O**, showing the severe disorder on the alkyl chain whereby the end atoms are missing. The disordered PF_6^- is shown. (b) Crystal packing of **R4(PF$_6$)·3H$_2$O**, the hydrogen atoms have been omitted for clarity.

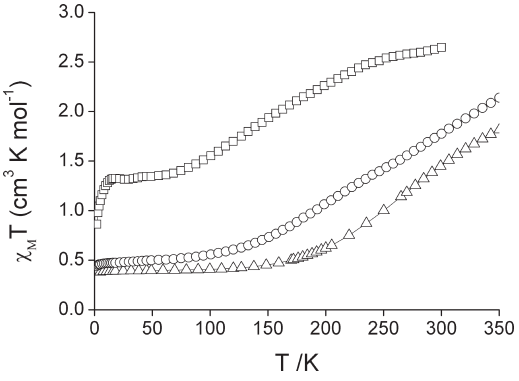

Figure 5. Plots of $\chi_M T$ versus temperature for polycrystalline powdered samples of **R4(BF$_4$)·H$_2$O** (△), **R8(BF$_4$)·H$_2$O** (○), and **R12(BF$_4$)·8.5H$_2$O** (□).

$\chi_M T$ value of 2.65 cm^3 K mol^{-1} at 300 K. With decreasing temperature the $\chi_M T$ values gradually decrease over the temperature range 300−70 K to reach a minimum value of 1.34 cm^3 K mol^{-1}, indicative of an incomplete LS character. Below 10 K, the moment decreases again, slightly, to 0.86 cm^3 K mol^{-1}, likely due to zero-field splitting of the HS ^4A state (derived from the $^4T_{1g}$ state in a distorted octahedral geometry) and not to a rapid spin or phase change. We note that such a decrease in $\chi_M T$ below 10 K was not seen in the fully HS $[Co(terpyOH)_2](PF_6)_2$ complex that showed a more gradual decrease, typical of HS magnetism, occurring below approximately 250 K,[10] but a decrease below 10 K was seen in $[Co(terpy)_2](ClO_4)_2 \cdot 0.5H_2O$ that displayed close to HS behavior.[6] The plateau value of $\chi_M T$ observed for **R12-(BF$_4$)·8.5H$_2$O** in the temperature interval 10−70 K is significantly larger than that expected for pure LS behavior and is indicative of the presence of a significant portion of HS molecules (ca. 40%). Thus, the longest chain analogue of the BF_4^- series displays a gradual spin transition which shows a decreased low temperature onset value (70 K) than the other analogues. The $T_{1/2}$ of approximately 145 K is significantly lower than the R4 and R8 analogues. As for the R4 and R8 derivatives no thermal hysteresis in the moment was observed.

The change in the chain length thus appears to have a subtle influence on the SCO behavior for the constant BF_4^- anion such that the low temperature onset values of the spin transition are decreased with increasing chain length and with decreasing $T_{1/2}$ values with increasing chain length. However, the disorder noted in the alkyl chains of some of the compounds, as well as in the anions, might well influence the spin crossover in individual compounds. We note, also, that with the differing degrees of hydration throughout this series, there is a large variation in the type and degree of hydrogen-bonding pathways, which are known to influence the SCO character; thus, further conclusions cannot be drawn at this time.

Because of the contributions of ligand-field distortions, spin−orbit coupling, and spin equilibrium to the observed $\chi_M T$ plots of Figure 5, we have not attempted to simulate them. Use of a thermal equilibrium model and a Boltzmann distribution between the LS and HS (single) levels of one Co(II) molecule, separated by energy gap, E,

of the kind given in ref 6 will yield E values of some hundreds of cm^{-1} with E decreasing in the order R4 > R8 > R12.[28]

Regarding the magnetism for ClO_4^-, PF_6^-, and BPh_4^- salts of the R4, R8, and R12 materials (Figures S7−S13) in all cases except for **R12(PF$_6$)·MeOH**, broad gradual spin crossover natures are observed as for the Co(II) terpyridone analogues and for the methanol-solvated R16 derivative but not, apparently, the R14 compound.[10,12] Contrasting this are the long alkyl-chain substituted phenanthroline and triazole derivatives of iron(II), which have shown both gradual and abrupt transitions perhaps indicative of stronger cooperativity in some cases.[11,14−16] Overall, in these series presented here we can see a number of general trends emerging. First, it appears that with increasing chain length, the degree of high spin character at low temperatures is increased, in particular for the R12 cases. This suggests that the longer alkyl chains, which are likely to be more mobile than the shorter chain analogues, allow more flexibility in the crystal lattice and hence are not energetically favorable for the fully low spin state to be attained. Second, it is evident that the BF_4^- and ClO_4^- anion containing materials, irrespective of chain length, tend to result in higher transition temperatures than the more bulky BPh_4^- and PF_6^- anion containing analogues. This may result from the increased numbers of intramolecular interactions possible with a more close packed nature of the smaller anions, thus enhancing communication pathways in the crystal lattice. Further conclusions cannot be drawn at this time as these materials contain differing degrees of solvation and indeed different solvent in some cases, which would also influence the spin crossover nature observed. Highlighting this is the methanol solvate **R12(PF$_6$)·MeOH**, which shows a complete HS character over all temperatures. Such a solvate dependence of the spin state and spin transition of this type has been reported for the related $[Co(terpyOH)_2](Y)_2 \cdot S$ family.[10]

EPR Spectroscopy

X-Band Frozen Solution Spectra. Spectra of frozen solutions were obtained with the objective of discriminating between those effects due to intermolecular interactions in the solid state and those largely due to the Co complexes themselves. The spectra of approximately 1 mM frozen solutions of **R4(BF$_4$)·H$_2$O**, **R8(BF$_4$)·H$_2$O**, and **R12(BF$_4$)·8.5H$_2$O** in $CHCl_3$ or DMSO over the temperature range from 2.5 K up to approximately 180 K ($CHCl_3$) and approximately 220 K (DMSO) were quite similar apart from differences in line width, are attributable only to low-spin Co(II), and are simulated with an orthorhombic spin Hamiltonian as described below. A typical frozen solution spectrum is shown as Figure 6c (see also Supporting Information, Figure S7). The differences between the frozen solution spectra can be attributed to differences in solute concentration, solute aggregation

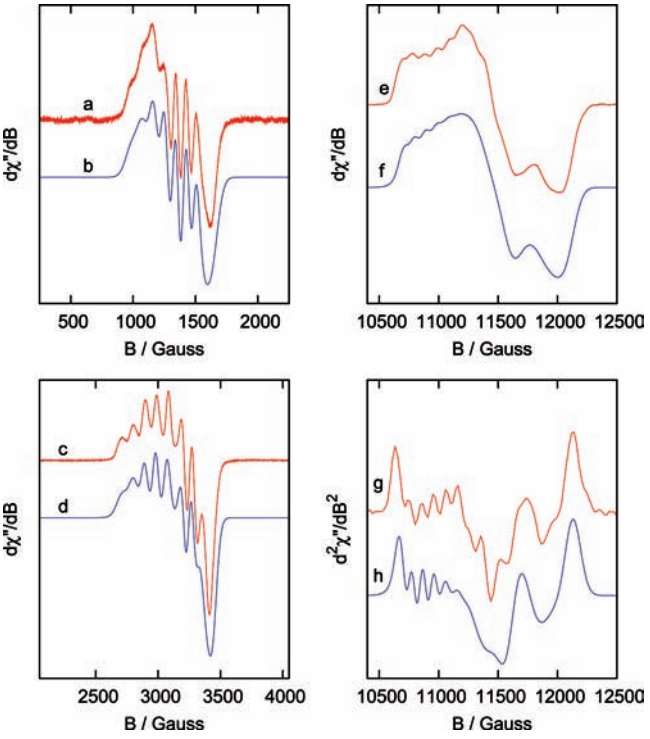

Figure 6. Multifrequency EPR spectra of **R8(BF$_4$)·H$_2$O** measured in chloroform. (a) Experimental and (b) simulated S-band spectra (ν = 4.038 GHz), T = 15.0 K; (c) experimental and (d) simulated X-band spectra (ν = 9.375 GHz), T = 25.0 K; (e) experimental and (f) simulated first derivative and (g) experimental and (h) simulated second derivative Q-band spectra (ν = 34.082 GHz, T = 6.07 K). Simulated spectra computed with the spin Hamiltonian and line width parameters, as in the text and Table 3.

(leading to poor glass formation), and variations in $g-A$ strain effects[29] and below approximately 30 K to a dependence of the spin relaxation time on the nuclear spin magnetic quantum number m_I. There appeared to be no correlation between the chain length and the temperatures below which resonances were observed.[30] No resonances could be observed from a solution of **R4(BF$_4$)·H$_2$O** in $CHCl_3$ when examined using an aqueous solution cell at approximately 240 K. Since the SCO phenomenon does not appear to occur in frozen solution (see below), we may conclude that the disappearance of the resonances in frozen solution is due to T_1 (spin−lattice) relaxation effects, a common occurrence for LS Co(II) complexes.

Multifrequency EPR Spectroscopy of R8(BF$_4$)·H$_2$O. The multifrequency EPR experiments and associated simulations were undertaken to obtain an accurate determination of the g and A values and the directional relationships between their principal axes. Solutions of 1 mM of **R8(BF$_4$)·H$_2$O** in $CHCl_3$ were chosen as the most

(28) A more complete model for spin equilibrium in distorted octahedral Co(II) d^7 systems, related to that given in ref 6 but using more energy levels deriving from spin−orbit and ligand field splittings, has been applied to plots of the type shown in Figure 5. Kennedy, B. J.; Fallon, G. D.; Gatehouse, B. M.; Murray, K. S. *Inorg. Chem.* **1984**, *23*, 580–588.

(29) Froncisz, W.; Hyde, J. S. *J. Chem. Phys.* **1980**, *73*, 3123–3131. Hyde, J. S.; Froncisz, W. *Ann. Rev. Biophys. Bioenerg.* **1982**, *11*, 391–417. Pilbrow, J. R. *J. Magn. Reson.* **1984**, *58*, 186–203.

(30) The temperatures at which the resonances appeared are affected both by the melting point of the solvent and experimental conditions such as the cold nitrogen gas flow rate through the insert dewar and whether a particular series of measurements at the various temperatures commenced with a well frozen solution (e.g., at 110 K) or from the liquid phase. Although the freezing point of $CHCl_3$ is ca. 210 K and that of DMSO ca. 290 K, motion of the solvent molecules would appear to occur well below these temperatures resulting in a less rigid glassy medium.

convenient for these experiments. Spectra were recorded at S-band (4.038 GHz and 15.0 K), X-band (9.375 GHz and 25.0 K), and Q-band (34.082 GHz and 6.07 K) frequencies, as shown in Figure 6. While Q-band frequencies provided greater g value resolution and enabled the three principal components of the g matrix to be determined, the frequency dependence of the distribution of g and A values produces larger line widths and thereby decreases the spectral resolution (compare Figure 6c,e). In contrast, at lower frequencies (S-band, Figure 6a), g value resolution is decreased (compare Figure 6a,c,e), the effect of g and A strain on the line width is reduced, and there is larger state mixing between the electron Zeeman and hyperfine interactions. All of these factors contribute to greater spectral resolution, enabling the complete Co (II) hyperfine matrix to be determined.

Simulations of the multifrequency EPR spectra used the XSophe-Sophe-XeprView computer simulation software suite[24] in conjunction with Octave to optimize the spin Hamiltonian and line width parameters by fitting the S-, X- and Q-band (first and second derivative) spectra simultaneously. Through selective weighting of the four spectra we were able to search the spin Hamiltonian and line width parameter space and show that noncoincident angles between the principal components of g and A were not required to adequately simulate the EPR spectra. In obtaining the unique set of orthorhombic spin Hamiltonian and line width parameters given below, it was important to fit not only the first derivative Q-band spectrum but also the second derivative spectrum as this provided better resolution of the Co(II) hyperfine structure. The spin Hamiltonian and line width parameters are given in Table 3, where the g_i and A_i have their usual meaning for an orthorhombic spin Hamiltonian and the line width is expressed as

$$\sigma_v^2 = \left[\sum_{i=x,y,z} (\sigma_{Ri}^2 + ((\sigma g_i/g_i)\nu_0(B) + (\sigma A_i)M_I)^2) l_i^2 g_i^2\right]/g^2$$

where σ_R is the residual line width, $\sigma g/g$ and σA are the distributions of the g and A values, respectively, and the l_i are the direction cosines relating the magnetic field to the principal axis system. The residual line widths are determined by T_1 and T_2 processes and unresolved Co hyperfine and N superhyperfine couplings. The magnitudes of the g values and the largest hyperfine interaction observed here are similar to those found by Kremer et al.[6] for single crystals of the parent low spin $[Co(terpy)_2](Y)_2 \cdot nH_2O$ complexes, although the other two hyperfine interactions appear to be quite different (Table 3). The labeling of the principal components of g and A matrices from the frozen solution EPR spectra follows the convention for an elongated tetragonal Co(II) system with the z axis being that of the smallest g value and the longest bond length, directed along the axis of elongation. As discussed below (see EPR Summary and Discussion) this labeling of the z axis is different to that used for the polycrystalline powders, as a result of the imposition of a compressive strain in the latter.

X-band Polycrystalline Powder Spectra. The EPR spectra of the polycrystalline powders of **R4(BF$_4$)·H$_2$O**, **R8-(BF$_4$)·H$_2$O**, and **R12(BF$_4$)·8.5H$_2$O** show resonances arising from the low-spin $S = 1/2$ ground state of Co (II). There were no indications at any temperature down to approximately 2.5 K of resonances attributable to high spin $S = 3/2$ Co(II). The polycrystalline powder spectra were generally less well resolved than their equivalents in frozen solution. This difference is at least in part due to dipolar and weak exchange interactions between neighboring Co(II) ions. The increased broadening as a function of temperature is likely to be due to faster T_1 processes (as with the frozen solutions), greater structural disorder, and the increased population of the HS state, although for the latter, the relative relaxation times of the LS and HS Co(II) ions will be important.

The best resolved X-band spectra of the polycrystalline powders were those obtained for **R8(BF$_4$)·H$_2$O** as shown in Figure 7. The spectrum at 4.5 K (Figure 7b) has a similar appearance to that of Figure 6c and was simulated using an orthorhombic spin Hamiltonian with similar parameters to those applicable for the frozen solution spectra. The spectrum of the polycrystalline powder at Q-band

Table 3. Spin Hamiltonian and Line Width Parameters for the Simulation of the Spectra of Figure 6

	g (±0.001)	$A \times 10^{-4}$ cm^{-1} (±0.05)	$\sigma_{Ri} \times 10^{-4}$ cm^{-1} (±1.0)	$\sigma g_i/g_i$	$\sigma A_i, \times 10^{-4}$ cm^{-1}
x	2.206	91.28	44.6	0.0029	−14.60
y	2.141	60.30	26.7	0.0142	22.32
z	2.033	36.42	33.5	0.0069	3.27

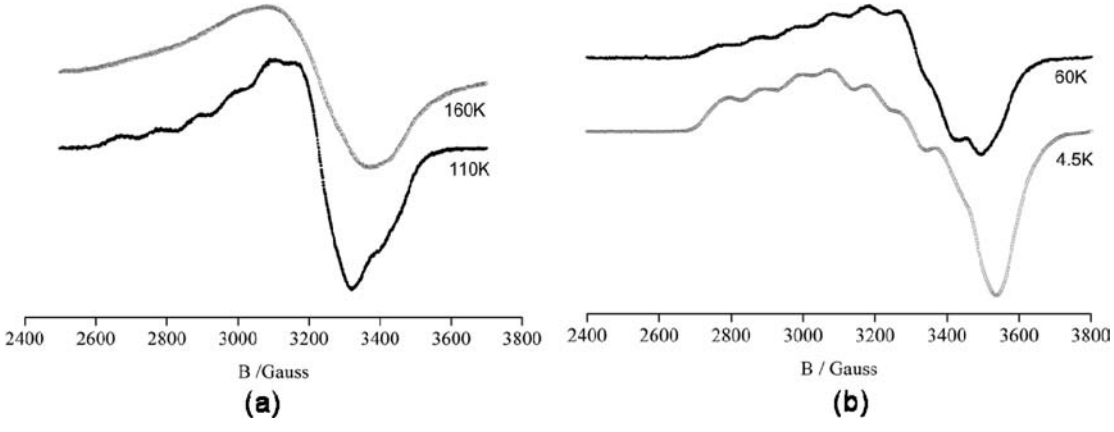

Figure 7. EPR spectra of polycrystalline powder of **R8(BF$_4$)·H$_2$O** at the temperatures indicated and microwave frequencies of (a) 9.431 GHz and (b) 9.707 GHz.

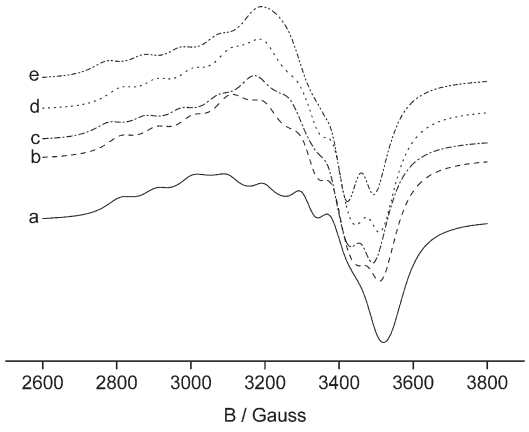

Figure 8. EPR spectra simulated using the g_i and A_i values shown in Table 4. The simulated spectra are similar to those of the experimental spectra for **R8(BF$_4$)·H$_2$O** in Figure 7, at 110, 60, and 4.5 K, but are not intended as an exact fit. Note that there is not a one to one correspondence between the spectra in Figure 7 and the simulated ones above. For all simulations: microwave frequency 9.707 GHz, Lorentzian line shape (cutoff = 10), line width 50×10^{-4} cm^{-1}; $g-A$ strain parameters $\sigma g_i/g_i = 0.001$, and $\sigma A = 0.10$. Units of $A_i \times 10^{-4}$ cm^{-1}.

(34.082 GHz) and 6 K was closely similar in appearance to that of the frozen solution spectra shown in Figure 6e.

As shown in Figure 7, the spectrum changes markedly with increasing temperature, taking on an axially symmetric appearance at around 110 K. Above about 130 K the hyperfine resonances could not be clearly distinguished, and at 160 K the spectrum consisted of a single asymmetric broad line of width approximately 300 G and a g value approximately 2.10. No resonances could be observed above approximately 200 K. The spectral simulations shown in Figure 8, although not intended to be an exact match with the experimental spectra of Figure 7, show the influence of the changing g and A values on the spectral line shape. The spin Hamiltonian and line width parameters used in these simulations are listed in Table 4. The similarities between the experimental spectra at 4.5, 60, and 110 K and the simulated spectra of Figure 8a,c,e, respectively, should be noted. It should also be noted that the labeling of the x and z axes of the g and A matrices for the polycrystalline powders in Tables 4 is opposite to that expected by convention and as used for the frozen solutions (Table 3). As discussed below (see EPR Summary and Discussion), this is a consequence of the compressive strain imposed by the crystal lattice on the Co(II)N$_6$ configuration.

Detailed simulations of the spectra of **R8(BF$_4$)·H$_2$O** gave values of the spin Hamiltonian parameters g_i and A_i ($i = x, y, z$) over the temperature range 3.2−130 K. At 3.2 K the values of g_i and A_i were (2.020, 2.135, 2.200) and (15, 50, 100) $\times 10^{-4}$ cm^{-1}, respectively. The temperature dependence of g_i is shown in Figure 9 where it can be seen that the largest g value, g_z, increases by about 10% and the two lower g values (g_x and g_y) converge toward their mean value (ca. 2.08) as the temperature increases from 3.2 K to approximately 130 K. While the poor resolution of the polycrystalline powder spectra at X-band resulted in only qualitative estimates of the hyperfine interaction parameters A_i being made over the same temperature range, the largest hyperfine interaction parameter, A_z, increased by about 10% from 98×10^{-4} cm^{-1} and the

Table 4. Plots of g values and Co hyperfine interactions for the simulated spectra of Figure 8. Hyperfine interaction parameters (A) are in units of 10^{-4} cm^{-1}. The line width and gA strain parameters used are given in Figure 8

symbol	g_x	g_y	g_z	A_x	A_y	A_z
a (solid line)	2.020	2.135	2.200	15	50	100
b (dashed line)	2.050	2.120	2.200	20	35	100
c (dashed dotted line)	2.055	2.110	2.220	20	30	100
d (dotted line)	2.060	2.105	2.220	15	30	102
e (dashed dotted dotted line)	2.080	2.090	2.220	15	25	104

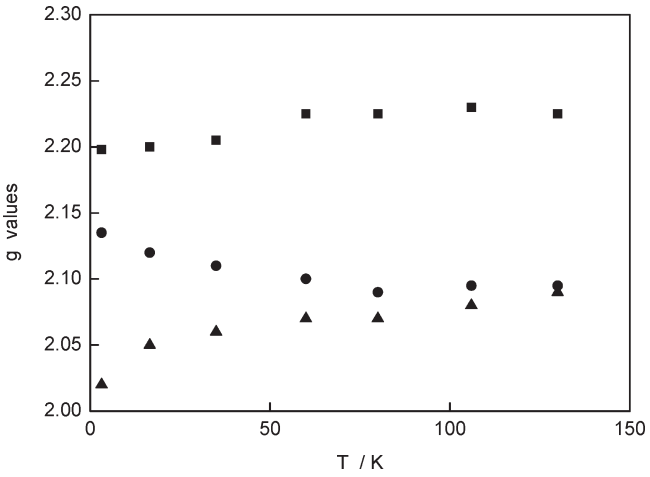

Figure 9. g values as a function of temperature for **R8(BF$_4$)·H$_2$O**. ▲, g_x; ●, g_y; ■, g_z.

smaller hyperfine interaction parameters (A_y and A_x) converged to a value in the range 10 to 20 $\times$ 10^{-4} cm^{-1}.

For [Co(terpyR4)$_2$](BF$_4$)$_2$·H$_2$O, **R4(BF$_4$)·H$_2$O**, a broad isotropic line of peak-to-peak derivative width around 500 G and centered around $g = 2.11$ was observed below approximately 250 K, as shown for 220 K in Figure 10a. This narrowed as the temperature was reduced, so that at around 110 K a feature was resolved on the low field side (Figure 10a), giving the appearance of an axially symmetric system. The spectrum showed little further change as the temperature decreased down to about 40 K but changed significantly below this temperature (Figure 10b) to give a spectrum with an orthorhombic appearance. The change from an axial to an orthorhombic appearance appeared to occur at a rather lower temperature than for **R8(BF$_4$)·H$_2$O**. As shown in Figure 10b, the 14 K spectrum exhibited poorly resolved features attributable to Co hyperfine structure and at 4.3 K was similar to that of **R8(BF$_4$)·H$_2$O** at the same temperature. Although the poorer resolution of the experimental spectra precluded simulations as accurate as those for **R8(BF$_4$)·H$_2$O** and therefore plots of the g values as a function of temperature similar to those of Figure 9, similar trends could be discerned (cf. plots c and a of Figure 8 with the spectra at 14 and 4.3 K of Figure 10). The spectrum at 3.7 K approached even more closely that of an axial configuration with the symmetry axis along g_x, with ($i = x, y, z$) g_i values estimated as (1.99, 2.17, 2.20) and A_i (15, 85, 90) $\times 10^{-4}$ cm^{-1}. Simulations of the spectra showed that the trends of converging g_x and g_y and increasing g_z with temperature shown in Figure 9 also occurred for **R4(BF$_4$)·H$_2$O**, with the average of g_x and g_y being estimated as 2.06 and the value of g_z being estimated

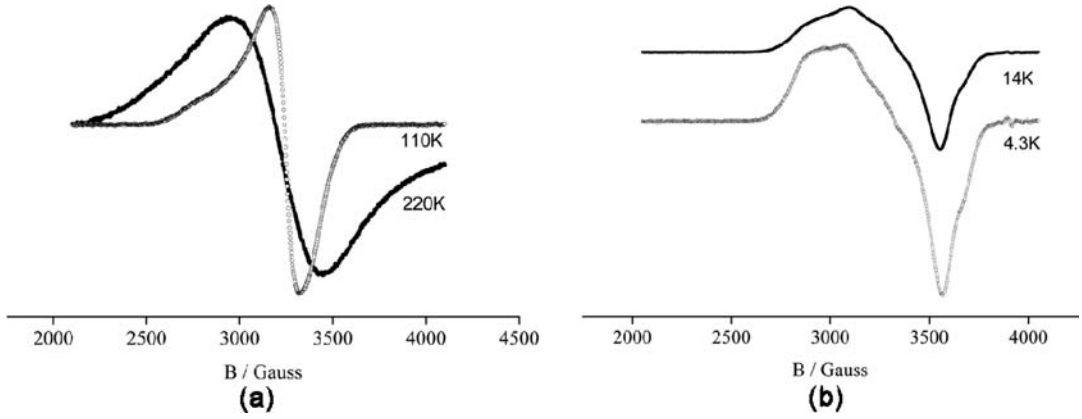

Figure 10. EPR spectra of polycrystalline powder of **R4(BF$_4$)·H$_2$O** at the temperatures indicated and microwave frequencies of (a) 9.436 GHz and (b) 9.720 GHz.

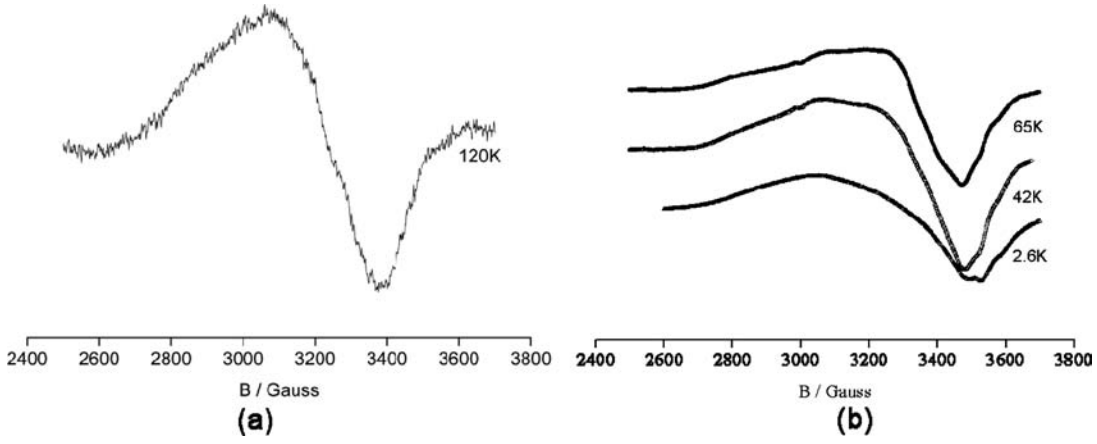

Figure 11. EPR spectra of polycrystalline powder of **R12(BF$_4$)·8.5H$_2$O** at the temperatures indicated and microwave frequencies of (a) 9.432 GHz and (b) 9.714 GHz.

as 2.40 (±0.05) at 110 K. The apparent symmetry axis is now along g_z (see discussion below).

For [Co(terpyR12)$_2$](BF$_4$)$_2$·8.5H$_2$O, **R12(BF$_4$)·8.5H$_2$O**, no resonances could be clearly observed above about 140 K. Although features attributable to Co hyperfine structure could be observed at approximately 65 K (see Figure 11b), these were poorly resolved even at 2.6 K. As with the other two complexes, the spectrum was temperature dependent. While accurate simulations were prevented by the large spectral line widths, these indicated that a distinctively orthorhombic spectrum (approximate g values g_x 2.06, g_y 2.09, g_z 2.24) was present even at 120 K, a rather higher temperature than that at which a clearly orthorhombic spectrum was observed for **R8(BF$_4$)·H$_2$O** or **R4(BF$_4$)·H$_2$O**. The g values at 2.6 K appeared to be more orthorhombic than those at a similar temperature for **R8(BF$_4$)·H$_2$O** or **R4(BF$_4$)·H$_2$O**, being g_i (x, y, z) 2.05, 2.11, and 2.20 respectively. The values of A_i were also orthorhombic, being (for $i = x$, y, z) estimated as 15, 60, and 100 × 10^{-4} cm^{-1}, again indicating a more orthorhombic character at this temperature than for **R8(BF$_4$)·H$_2$O** or **R4(BF$_4$)·H$_2$O**.

Does a Spin Crossover Occur in Frozen Solution? An indirect answer to this question was obtained by considering the temperature dependence of the EPR spectral intensities as a function of temperature. Since the resonances are due only to low-spin Co(II) with $S = 1/2$, a departure from linearity of plots of the spectral intensities, I (obtained through double integration of the first derivative spectra) as a function of $1/T$ or of $I \times T$ as a function of T (where T is the temperature) may be taken as being due to a change in the population of the $S = 1/2$ state and thus an indicator of SCO behavior. For consistency with the magnetic susceptibility measurements shown in Figure 5, $I \times T$ was initially plotted as a function of T for both high (105 K to ca. 220 K) and low (2.5 K to ca. 80 K) temperature ranges. Because the temperature is included explicitly in both the $I \times T$ and T axes, significant scatter results from uncertainties in its measurement. Although this scatter was not significant for the high temperature range, the uncertainties in the low temperature range were such that no meaningful conclusions could be drawn. The uncertainties in the temperature measurement have a less profound effect on plots of I vs $1/T$, and such plots were therefore chosen to represent the low temperature range.

For the frozen solutions, a linear relationship was found for plots of $I \times T$ versus T from 105 K up to the temperature above which the frozen solution was no longer a good glass (ca. 180 K for $CHCl_3$ and ca. 220 K for DMSO (Figure 12 and Supporting Information, Figures S8 and S9). Data for the frozen solutions in the low temperature range were limited, but where available the plots of I vs $1/T$ were linear for temperatures from

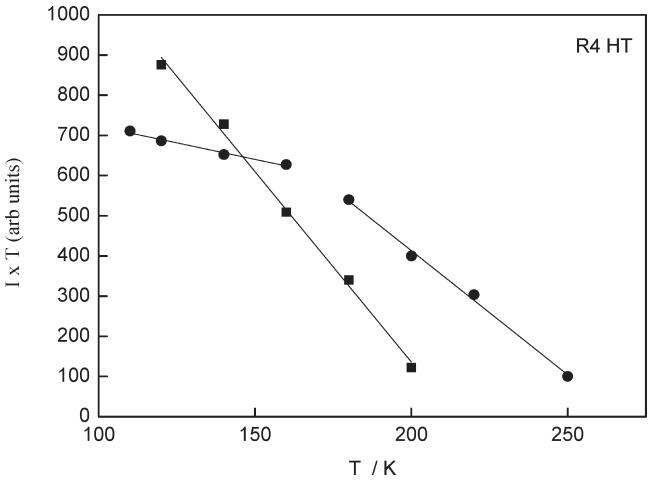

Figure 12. Integrated intensity (I) $\times$ T as a function of T for **R4(BF$_4$)·H$_2$O** in the high temperature region. ■, frozen DMSO solution; ●, polycrystalline powder.

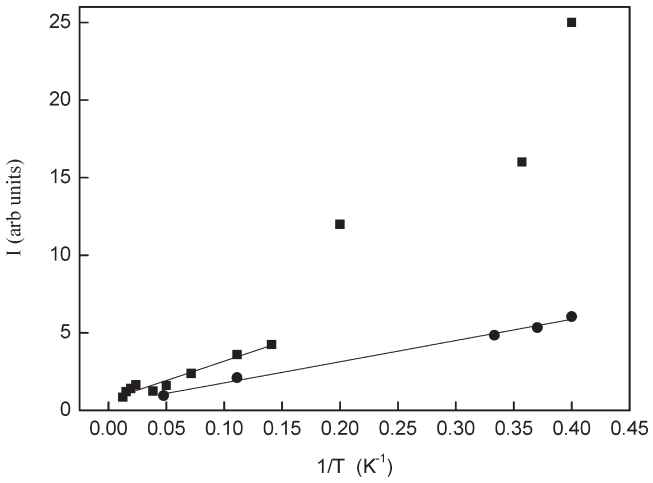

Figure 13. Integrated intensity, I, as a function of $1/T$ for **R12(BF$_4$)·8.5H$_2$O** in the low temperature region. ●, frozen DMSO solution; ■, polycrystalline powder.

2.5 K up to around 25 K (Figure 13 and Supporting Information, Figures S10 and S11).

As shown in Figure 12, the plot of $I \times T$ vs T for the polycrystalline powder of **R4(BF$_4$)·H$_2$O** in the range 105 K to around 250 K exhibited nonlinear behavior. This is attributed to a decreasing population of the LS $S = 1/2$ state and the increasing population of the HS $S = 3/2$ state which does not contribute to the EPR spectrum. This is consistent with the magnetic susceptibility measurements of Figure 5 which indicate the onset of the SCO phenomenon in this temperature range. Since the plot for the frozen solution of **R4(BF$_4$)·H$_2$O** in DMSO shows no departure from linearity over a similar temperature range, we may conclude that SCO does not occur in dilute frozen solutions of **R4(BF$_4$)·H$_2$O**.

Data for the polycrystalline powders of **R8(BF$_4$)·H$_2$O** and **R12(BF$_4$)·8.5H$_2$O** for the temperature range above 105 K were limited because resonances were not observed above 180 and 160 K, respectively. Although the commencement of a similar trend to that for **R4(BF$_4$)·H$_2$O** could be discerned for **R8(BF$_4$)·H$_2$O** up to about 140 K, there was insufficient data to draw any conclusions for **R12(BF$_4$)·8.5H$_2$O.**

Plots of I as a function of $1/T$ for the polycrystalline powders in the low temperature range (80 K down to 2.5 K) are shown in Figures 13 and Supporting Information, Figures S10 and S11. There appeared to be no significant departure from the linear dependence of intensity with $1/T$ for **R4(BF$_4$)·H$_2$O** and **R8(BF$_4$)·H$_2$O**, although the plot for **R12(BF$_4$)·8.5H$_2$O** showed a more rapid than linear increase in intensity as the temperature was reduced below about 10 K. This is just the region where the magnetic moment decreases sharply (Figure 5), attributed to depopulation of one of the doublets of the spin quartet of the HS state. The more rapid increase in EPR spectral intensity below 10 K is then attributable to the increasing population of the LS state. Since no corresponding changes were observed for the spectral intensities of the frozen solution, we deduce that for **R12(BF$_4$)·8.5H$_2$O** also, SCO does not occur in frozen solutions.

EPR summary and discussion. In summarizing the EPR spectroscopy, we note that the spectra observed for both frozen solutions and polycrystalline powders are due only to Co(II) ions in the LS state with $S = 1/2$. The spectra of the frozen solutions exhibit orthorhombic symmetry and are essentially independent of temperature, chain length, and solvent. The spectral intensities vary linearly as a function of $1/T$, indicating that there is no significant population of the high spin state. In contrast, the spectra of the polycrystalline powders followed a trend from orthorhombic to axial and finally to isotropic with increasing temperature, with the orthorhombic character of the spectra persisting to higher temperatures for the longer chain lengths. The temperature below which resonances are observed for the polycrystalline powders depends markedly on the chain length, being lower for the longer chain lengths, in parallel with the trend for the SCO temperature $T_{1/2}$. In contrast to the frozen solutions, the temperature dependence of the spectral intensities of the polycrystalline powders show evidence for the population of the HS $S = 3/2$ state and hence for SCO phenomena even though HS resonances could not be detected.

In the discussion below, we concentrate on the interpretation of the spectra of **R8(BF$_4$)·H$_2$O** as being the most complete and best characterized data set. The same general interpretation applies to both **R4(BF$_4$)·H$_2$O** and **R12(BF$_4$)·8.5H$_2$O** but with some differences in detail.

It is generally accepted that, for a six-coordinate LS Co(II) complex with O_h symmetry, the single unpaired electron will be in the degenerate e_g orbitals. A consequence of the Jahn−Teller theorem is to remove this degeneracy by inducing an elongative or compressive distortion of the Co−ligand bonds parallel to one of the three orthogonal axes.[31] The elongated configuration is energetically preferred, and the single unpaired electron will be in a 3d(z^2) orbital, with the z-axis being the axis of elongation.[32] In the dynamic Jahn−Teller case which

(31) For a general discussion of the Jahn−Teller effect see: Pilbrow, J. R. *Transition Ion Electron Paramagnetic Resonance*; Clarendon Press: Oxford, 1990; Chapter 2, pp 102−114. Abragam, A.; Bleaney, B. *Electron Paramagnetic Resonance of Transition Ions*; Clarendon Press: Oxford, 1970; Chapter 21.

(32) See for example Purcell, K. F.; Kotz, J. C. *Inorganic Chemistry*; W B Saunders Company: Philadelphia, 1977; Chapter 9, pp 556−559.

occurs when all six ligands are identical, there are three equivalent minima, each corresponding to an elongation along one of the orthogonal axes, and the direction of distortion is able to fluctuate between all three orthogonal axes. The three equivalent minima of the E⊗e Jahn−Teller surface give rise to what is often described as a "warped Mexican hat" potential energy surface. At higher temperatures, the rate of tunneling between the minima is rapid enough to give a dynamical averaging of the spectrum similar to that observed for "tumble averaged" liquid phase spectra.[33] At low temperatures, where the fluctuations are slower than the EPR observation time (ca. 10^{-10} s), a "static" picture of the molecule trapped within a single minimum is presented.

The temperature independence of the spectra of the frozen solutions indicates that the static picture applies, with the molecules being trapped in a single minimum. The z-axis is defined as that of the elongation and is the high symmetry direction. Simple ligand field theory then predicts that the g values for this static elongated geometry with a $d(z^2)$ ground state should be $g_x \geq g_y > g_z \approx 2.00$. The g values as labeled in Table 3 are consistent with this labeling of the axes, with g_y being closer to g_x than to g_z. Although the relative magnitudes of the hyperfine interactions are opposite to those expected from simple theory, it has been shown[34] that this is inadequate for LS Co(II) d^7. As pointed out by McGarvey, the admixture of other states affects the hyperfine interactions to the second order but the g values only in the third order.[35] The relative magnitudes and signs of the various contributions from other states and the core polarization terms have a significant influence on the magnitudes and signs of the components of the hyperfine matrix, as can be seen from the simplified expressions given by Pilbrow and Winfield.[34] Similar g and A values to those found here for the elongated configuration for low spin Co(II) have been found for an octahedrally compressed configuration of the $CuCl_4(NH_3)_2^{2-}$ center in NH_4Cl where the ground state is also primarily $d(z^2)$.[36]

The simple picture described above for the frozen solutions is inadequate for the polycrystalline powders. A more appropriate picture takes account of the effects of the perturbations of the "warped Mexican hat" potential surface induced by the lowering of the site symmetry as a result of inequivalence of the ligands or of distortions imposed by the lattice in the solid state. An important case that is wellknown to give rise to temperature dependent EPR spectra occurs when the low symmetry perturbation acts as a tetragonal compression, in opposition to a "warped Mexican hat" surface where the minima are at elongated geometries. For very large values of the compression, the molecule will be stabilized at a single minimum at a compressed geometry. Temperature dependent EPR spectra then result from the lowering of the energy of the orthorhombic component of the Jahn−Teller vibration. A much more dramatic temperature dependence occurs when the strain perturbation (S_θ) and the barrier height (2β) between the "warped Mexican hat" potential minima fulfill the condition $|S_\theta| < 9\beta$.[37] In this case two of the minima are lowered in energy with respect to the third. The degeneracy of the two lower minima is removed by any orthorhombic component of the low symmetry perturbation. Another consequence of the tetragonal compression is that these two minima which corresponded to elongations along the x and y molecular axes in the "warped Mexican hat" surface actually become orthorhombic. One minimum has $r_x \gg r_y > r_z$, and the other has $r_y \gg r_x > r_z$, essentially an interchange of the x and y axes, with the z-axis for both minima being along that of S_θ. In the spectra given in Figure 9, we have labeled the low temperature g value $g_x \ll g_y < g_z$, as in our description the geometry of the lowest vibronic level corresponds to a tetragonal elongation along r_x (with an orthorhombic distortion). Although this appears to be an unusual notation, it provides the basis for a unifying explanation of the temperature dependence of the g values and reflects the influence of a dominant tetragonal compression along z imposed on the "warped Mexican hat" surface by the low symmetry crystal environment.

The temperature dependence of the EPR spectra of the polycrystalline powders can now be explained in a qualitative fashion. The description parallels that used in the quantitative description of the behavior of a number of Cu(II) complexes.[38−40] On this model, at temperatures below 4 K, the lowest energy minimum will contain the bulk of the population and the EPR spectrum will have the appearance of an approximately elongated tetragonal configuration with the symmetry axis along the x-direction. As the temperature increases, the next highest minimum, corresponding to the configuration with the longest bonds along the y-direction, becomes progressively populated. If the rate of exchange between the populated levels is fast compared to the EPR time scale, the observed EPR spectrum is one in which the g and A values are averaged along the x, y, z directions rather than a superposition of the spectra for each level. In these circumstances, the observed bond lengths along the x and y directions appear to approach the average of their low temperature values, leaving the z-axis, the direction of the axial component of the compressive strain S_θ, as the apparent symmetry axis. Since this is the direction of the shortest bond length and the largest g and hyperfine values, the appearance given by the X-ray crystallographic structure and the EPR spectra is that of a tetragonal compression along the z-axis. This apparent switch of the approximate tetragonal axis of symmetry from an elongation along the x-axis to a compression along the z-axis with increasing temperature is often seen in copper(II) complexes.[38−41] On increasing the temperature even further, the highest energy minimum will begin to populate, and the averaging of all three minima will lead to an isotropic EPR spectrum and the impression of approximately equal bond lengths.

(33) Abragam, A.; Bleaney, B. *Electron Paramagnetic Resonance of Transition Ions*; Clarendon Press: Oxford, 1970; Chapter 7, pp 465−466.
(34) Pilbrow, J. R.; Winfield, M. E. *Mol. Phys.* **1973**, *25*, 1073–1092.
(35) McGarvey, B. R. *Can. J. Chem.* **1975**, *53*, 2498–2511.
(36) Pilbrow, J. R.; Spaeth, J. M. *Phys. Status Solidi* **1967**, *20*, 225−235 and 237−248.
(37) Reinen, D.; Krause, S. *Inorg. Chem.* **1981**, *20*, 2750–2759.
(38) Riley, M. J.; Hitchman, M. A.; Mohammed, A. W. *J. Chem. Phys.* **1987**, *87*, 3766–3778.
(39) Simmons, C. J.; Stratemeier, H.; Hanson, G. R.; Hitchman, M. A. *Inorg. Chem.* **2005**, *44*, 2753–2760.
(40) Hadler, K. S.; Kilmartin, J. R.; Hanson, G. R.; Hitchman, M. A.; Simmons, C. J.; Riley, M. J. *Inorg. Chem.* **2008**, *47*, 8188–8196.
(41) Halcrow, M. A. *Dalton Trans.* **2003**, 4375–4384.

However, as pointed out by, for example, Halcrow,[41] the time scale of both the EPR measurements and the determination of bond lengths by X-ray crystallography may be significantly influenced by the dynamical averaging that results from the rapid exchange between different minima. A more correct picture is obtained by EXAFS measurements which have a much shorter time scale. An example of the effect of the dynamical averaging of bond lengths on the perception of the local structure is the case of $[(HC(Ph_2PO)_3)_2Cu](ClO_4)_2 \cdot 2H_2O$, where the bond lengths and structure as determined by EXAFS suggested that the elongated tetragonal configuration exhibited at low temperatures was retained even at 298 K.[42] A similar situation would appear to apply to the Co(II) complexes studied in this paper, so that on the EXAFS time scale, the present complexes have an elongated tetragonal configuration at all temperatures, with the direction of elongation being along one of the three orthogonal axes. The compressed tetragonal structure observed by X-ray crystallography and the axially symmetric EPR spectrum, both with their axis of symmetry along the direction of compression, result from the dynamical averaging of two elongated tetragonal configurations with their directions of elongation perpendicular to the direction of the axial component of the compressive strain.

Regarding the complexes discussed in this paper, the *g* values of **R4(BF$_4$)·H$_2$O** at 3.7 K in particular and of **R8(BF$_4$)·H$_2$O** at 3.2 K, although orthorhombic, have an approximate tetragonally elongated axis associated with the lowest *g* value, as the high two *g* values are closer than the lower two. At around 120 K, both **R4(BF$_4$)·H$_2$O** and **R8(BF$_4$)·H$_2$O** exhibit an apparently axial spectrum, but with the high symmetry direction now being associated with the highest *g* value. These spectra are consistent with the X-ray crystallographic structures obtained at 123 K which show a compressed tetragonal configuration (see, e.g., Figure 3 and Table 2 for **R8(BF$_4$)·H$_2$O**). The isotropic spectrum observed at even higher temperatures, for example, for **R4(BF$_4$)·H$_2$O** (Figure 10, 220 K) and approached by **R8(BF$_4$)·H$_2$O** (Figure 7, 160 K) is then the consequence of the thermal equilibrium being between all three wells of the Mexican hat potential surface.

The differences between the spectra at specified temperatures and in their temperature dependence implies that the chain length has a significant influence on the magnitudes of the strain components. The chain length also has a significant influence on the manifestation of the SCO phenomenon. Thus, there would appear to be a relationship between the lattice strain and the onset of spin crossover. While in the present interpretation the low symmetry strain parameters are assumed to be temperature independent, there are likely to be cooperative effects in these pure Co(II) compounds that may modify the simple model. However, quantitative formulation of such effects and of the relationship between the magnitudes of the low symmetry strain parameters and SCO behavior was considered to be beyond the scope of this paper.

Conclusions

A family of $[Co(II)(terpyRX)_2](Y)_2$ type materials has been synthesized where the alkyl chain length and counteranion have been systematically varied to elucidate any potential structure and magnetic relationship. We note, also, that these compounds have been obtained recently by a most unusual route that involved reaction of a ditopic ether-linked *bis*-terpy Co(II) polymer with an alcohol, ROH, with the $[Co(terpyRX)_2](PF_6)_2 \cdot MeCN$ structures being solved for X = 1 and 2.[43] Although the X-ray crystallographic and EPR evidence implies that, at 120 K, the LS Co(II) centers of the materials structurally characterized within this series are in compressed octahedral environments, the EPR studies over the temperature range from 2.5 to 250 K reveal that in each case the observed behavior is due to a dynamic averaging of vibronic energy levels. The levels are at the geometries of three minima, each of which has essentially an elongated tetragonal geometry along a different axis. The absence of both SCO behavior and strain effects in the EPR of frozen solutions and their presence in the polycrystalline powders suggest a relationship between the lattice strain and the SCO behavior. Within the present series of complexes, magnetic susceptibility studies showed incomplete spin transitions for all materials, with the exception of one PF_6^- salt that remained HS. When looking at the series of terpyRX complexes containing BF_4^- salts, a trend was observed such that the onset temperature of the SCO decreased with increasing alkyl chain length. On the other hand, the analogous families of ClO_4^-, BPh_4^-, and PF_6^- salts did not show as clearcut trends.

Acknowledgment. The authors are grateful to the Australian Research Council for Discovery and Linkage International Grants (to K.S.M.) that allowed P.N. to visit Monash University. P.N. also thanks the University of Southern Denmark, Faculty of Science, Odense, for support. We thank Dr. Michael Hitchman (University of Tasmania) and Dr. Malcolm Halcrow (University of Leeds) for their comments on aspects of X-band EPR spectra.

Supporting Information Available: Tables and Figures of crystallographic data (Tables S1−S4, Figures S1−S6); table of IR and Raman band positions (Table S5); EPR of frozen solutions (Figure S7), EPR intensity plots (Figures S8−S11), and figures of magnetic moments vs temperature for complexes with other anions (Figures S12−S20). This material is available free of charge via the Internet at http://pubs.acs.org.

(42) Masters, V. M.; Riley, M. J.; Hitchman, M. A.; Simmons, C. *Inorg. Chem.* **2001**, *40*, 4478–4480.

(43) Constable, E. C.; Harris, K.; Housecroft, C. E.; Neuburger, M.; Schaffner, S. *Chem. Commun.* **2008**, 5360–5362.